



The multiscale mechanics of axon durotaxis

Christoforos Kassianides^a, Alain Goriely^{a,*}, Hadrien Oliveri^b

^a Mathematical Institute, University of Oxford, Oxford OX2 6GG, United Kingdom

^b Max Planck Institute for Plant Breeding Research, Cologne 50829, Germany

ARTICLE INFO

Keywords:

Axons
Axon guidance
Durotaxis
Growth
Neurodevelopment
Morphoelasticity

ABSTRACT

During neurodevelopment, neuronal axons navigate through the extracellular environment, guided by various cues to establish connections with distant target cells. Among other factors, axon trajectories are influenced by heterogeneities in environmental stiffness, a process known as *durotaxis*, the guidance by substrate stiffness gradients. Here, we develop a three-scale model for axonal durotaxis. At the molecular scale, we characterise the mechanical interaction between the axonal growth cone cytoskeleton, based on molecular-clutch-type interactions dependent on substrate stiffness. At the growth cone scale, we spatially integrate this relationship to obtain a model for the traction generated by the entire growth cone. Finally, at the cell scale, we model the axon as a morphoelastic filament growing on an adhesive substrate, and subject to durotactic growth cone traction. Firstly, the model predicts that, depending on the local substrate stiffness, axons may exhibit positive or negative durotaxis, and we show that this key property entails the existence of attractive zones of preferential stiffness in the substrate domain. Second, we show that axons will exhibit reflective and refractive behaviour across interface between regions of different stiffness, a basic process which may serve in the deflection of axons. Lastly, we test our model in a biological scenario wherein durotaxis was previously identified as a possible guidance mechanism *in vivo*. Overall, this work provides a general mechanistic theory for exploring complex effects in axonal mechanotaxis and guidance in general.

1. Introduction

The establishment of the neuronal network is a fundamental event in neurodevelopment in which neurons send out slender processes, called *axons*, to meet other target cells – e.g. other neurons – and physically interconnect with them. During this process, the axons migrates through the extracellular environment towards its functional target, guided by a combination of environmental cues, including gradients in chemical or mechanical properties in their environment. This general process defines *axon guidance*.

A developing axon is composed of two main parts (see Fig. 1): the *axonal shaft*, a long filament-like section that contains the axoplasm made up of parallel microtubules cross-linked through microtubule-associated tau proteins, neurofilaments, and actomyosin; and the *growth cone*, a lamellipodium-like, actin-supported structure located at the tip of the axonal shaft (Franze, 2020; Oliveri and Goriely, 2022). The growth cone performs both locomotory and sensory functions and, thus, plays a key role in pathfinding. Historically, the focus has been mostly on *chemotaxis*, the guidance of axons by gradients in the concentration of diffusing chemicals (Mortimer et al., 2008). The underlying mechanisms and molecular actors of chemotaxis are relatively well

* Corresponding author.

E-mail address: goriely@maths.ox.ac.uk (A. Goriely).

<https://doi.org/10.1016/j.jmps.2025.106134>

Received 30 December 2024; Received in revised form 21 February 2025; Accepted 26 March 2025

Available online 5 April 2025

0022-5096/© 2025 The Authors. Published by Elsevier Ltd. This is an open access article under the CC BY license (<http://creativecommons.org/licenses/by/4.0/>).

Table 1
List of symbols.

Symbol	Meaning	Dimension
f	Cross-linker tension	$F = MLT^{-2}$
f_0	Cross-linker characteristic detachment force	F
x	Cross-linkers extension	L
κ	Spring constant of cross-linkers	FL^{-1}
κ'	Effective substrate stiffness	FL^{-1}
$\chi = \kappa' / \kappa$	Dimensionless substrate stiffness	Dimensionless
χ^*	Optimal (dimensionless) substrate stiffness	Dimensionless
k_{off}	Cross-linkers off-rate	T^{-1}
k_{on}	Cross-linkers on-rate	T^{-1}
ρ	Density of bound cross-linkers	L^{-1}
v	Extension speed of bound cross-linkers	LT^{-1}
c_{free}	Concentration of free cross-linkers	L^{-3}
\mathcal{V}	Typical volume of binding reactions	L^3
$s_0 = \mathcal{V}k_{\text{on}}c_{\text{free}}$	Attachment rate of cross-linkers	T^{-1}
B	Kinetic binding rate of cross-linkers	$L^{-1}T^{-1}$
U	Kinetic unbinding rate of cross-linkers	$L^{-1}T^{-1}$
T	Traction force exerted by an actin filament	F
M	Myosin contraction force	F
V	Actin filament velocity relative to the substrate	LT^{-1}
N	Total number of bound cross-linkers	Dimensionless
N^*	Total number of bound cross-linkers at optimal stiffness	Dimensionless
$K = s_0 / k_{\text{off}}$	Binding constant of cross-linkers	Dimensionless
ℓ	Typical cross-linker extension length	L
$q = f_0 / \kappa \ell$	Bond strength parameter	Dimensionless
$v = V / k_{\text{off}} \ell$	Dimensionless actin velocity	Dimensionless
Ξ	Friction coefficient between actin and cytoplasm	FTL^{-1}
$\xi = k_{\text{off}} \Xi / f_0 / \kappa$	Friction force scale between actin and cytoplasm	F
$r^* \approx 0.387$	Argument of the maximum of \mathcal{H} ; see (16)	Dimensionless
φ_0	Growth cone opening angle	Dimensionless
ρ	Density of focal adhesion at growth cone periphery	L^{-1}
$\mathbf{r} = (x, y)$	Position of the growth cone	L
θ	Orientation angle of the axon shaft	Dimensionless
\mathbf{t}	Tangent vector to the growth cone axis	Dimensionless
\mathbf{t}^\perp	Normal vector to the growth cone axis	Dimensionless
S_0, S, s, σ	Arclength parameters in the various configurations	L
$\boldsymbol{\tau}$	Unit tangent vector to the axon shaft	Dimensionless
$\boldsymbol{\tau}^\perp$	Unit normal vector to the axon shaft	Dimensionless
m	Internal moment in the axon shaft	FL
$\mathbf{n} = (n_x, n_y)$	Internal resultant force in the axon shaft	F
$n = \mathbf{n} \cdot \boldsymbol{\tau}$	Internal longitudinal force in the axon shaft	F
λ	Stretch ratio of the axon shaft	Dimensionless
γ	Growth stretch factor	Dimensionless
α	Axon shaft elastic stretch ratio	Dimensionless
η	Morphoelastic viscosity	FT
τ_k	Timescale of curvature remodelling	T
n_0	Threshold tension for growth	F
B	Bending stiffness of the axon shaft	FL^2
\mathcal{K}	Longitudinal stiffness of the axon shaft	F
$\mathbf{b} = (b_x, b_y)$	Friction force density between axon and substrate	FL^{-1}
ζ	Friction coefficient between axon and substrate	FTL^{-2}
$\mathcal{Z} = B\zeta / \mathcal{K}\eta$	Ratio of adhesion to viscosity effects	Dimensionless
\mathcal{L}	Characteristic bending length	L
Λ	Characteristic growth length	L
F	External force applied to axon tip	F
c	Axon growth speed	LT^{-1}
k	Curvature of the axon	L^{-1}
\hat{k}	Intrinsic curvature of the axon	L^{-1}
$\hat{\mathbf{r}}$	Position of the axon clamp	L
$\hat{\mathbf{t}}$	Tangent vector to the axon at the clamp	Dimensionless
$\hat{\mathbf{v}}$	Normal vector to the axon at the clamp	Dimensionless
$\hat{\theta}$	Axon angle w.r.t. the horizontal at base of dynamic section	Dimensionless
W	Axon shaft elastic energy density	F
$\alpha_T = T_2 / T_1$	Traction ratio at an interface	Dimensionless
β	Deflection index at an interface	Dimensionless

described, and have been featured in numerous models (Oliveri and Goriely, 2022). In contrast, *durotaxis*, the directed motion of cells along gradients in extracellular matrix stiffness (Shellard and Mayor, 2021; Espina et al., 2022), has been identified in axons mostly in the last decade and is only partially understood.

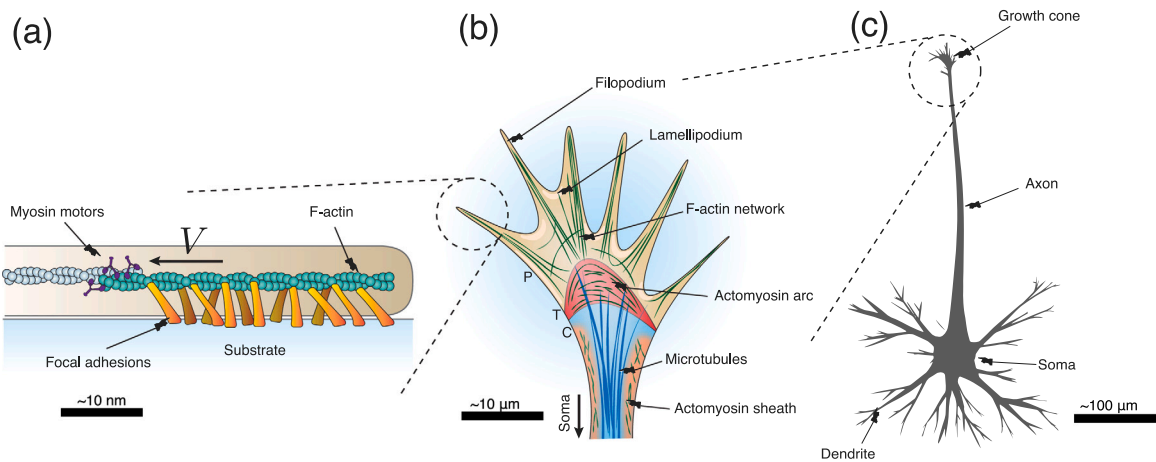


Fig. 1. The multiscale structure of the axon. (a) Molecular scale. An actin filament is pulled towards the rear of the growth cone by myosin motors. Actin is coupled mechanically to the substrate via transmembrane adhesive proteins which may detach and attach, producing an overall frictional force. This frictional force is key for axon locomotion. (b) Growth cone scale: schematic representation of the cytoskeleton in a migrating neurite. The shaft (lower part) is essentially composed of cross-linked microtubules surrounded by an actomyosin sheath. The growth cone is a lamellipodium-like structure that confers motility to the neurite and probes the environment. (c) Cellular scale. Schematic of a typical growing neuron showing the soma, the dendrites, and the axon with its growth cone.

For example, experiments on xenopus optic nerve guidance have suggested the existence of *negative* durotaxis, i.e. migration down the stiffness gradient, from high to low stiffness (Koser et al., 2016; Thompson et al., 2019). In an apparent contradiction, the same group observed that retinal axons also progress faster on *stiffer* regions (see Fig. 6 in Koser et al., 2016). At the scale of an entire axon fascicle, this effect then results in differential migration speed, hence a deflection of the axonal bundle towards *softer* regions, akin to the bending of light rays in a graded refractive medium (Oliveri et al., 2021). Similarly, axons in chick embryos grow towards softer zones of the somitic segments, strikingly, even in the context of inhibited chemotactic signalling (Schaeffer et al., 2022; Sáez and Venturini, 2023). Although mounting evidence supports the presence of neuronal durotaxis in vivo, its specific role and underlying mechanisms remain unclear.

By definition, durotaxis is a mechanics-based mechanism. Hence, a complete description of durotaxis must include the mechanical effects underlying growth and locomotion. The precise nature and mechanism of axonal growth have been long debated and remain controversial (Franze, 2020; Oliveri and Goriely, 2022; Suter and Miller, 2011). Generically, *growth* refers to the general process by which a body changes form by virtue of a change in mass (Goriely, 2017). In axons, the emerging view is that traction forces generated by the growth cone create mechanical tension along the trailing shaft; the latter then elongates in response to these forces (O'Toole et al., 2008; Suter and Miller, 2011; Nguyen et al., 2013; Holland et al., 2015; Goriely et al., 2015; Recho et al., 2016; Purohit and Smith, 2016; Miller and Suter, 2018; Franze, 2020; Oliveri and Goriely, 2022; Oliveri et al., 2022). Thus, we define *axonal growth* as the irreversible elongation of the axonal shaft resulting from these traction forces and supported by material addition. Microscopically, the mechanical forces generated by the growth cone arise from the mechanical coupling between the growth cone's actomyosin network and the substrate (Chan and Odde, 2008; Franze, 2020; Isomursu et al., 2022; Raffa, 2023). The effect of matrix compliance in this process can be understood through the so-called *molecular-clutch hypothesis* (Elosegui-Artola et al., 2018). Within the growth cone, actin undergoes a sustained retrograde flow, from the periphery of the growth cone to the base, generated by active myosin motors located at the base of the growth cone. This actin flow, in turn, generates micro-frictional interactions between the actin and the substrate, mediated by transmembrane adhesion complexes that may form and detach stochastically.

Overall, our general problem is to establish a physical law of motion for axons embedded in a heterogeneous mechanical environment. Here, we focus on two main problems. The first problem is to understand how these molecular interactions between substrate and axon result in the generation of an overall force. Then, from the molecular mechanics of growth cone locomotion, the second problem is to understand how this force affects the overall trajectory of the axon.

To address these problems, we develop a multiscale, mechanical model for axonal durotaxis, summarised in Fig. 2. We start with the molecular scale by describing the mechanical balance of a single actin filament interacting with a substrate (Section 2) and we derive the one-dimensional locomotory force resulting from this interaction. At the mesoscale (Section 3), we integrate the contributions of all actin filaments forming the growth cone actomyosin meshwork to compute the net force produced by the growth cone. Finally, at the macroscale (Section 4), this growth cone locomotory force is integrated in a rod theory to predict the trajectory of the whole axon.

Important physical quantities are listed in Table 1.

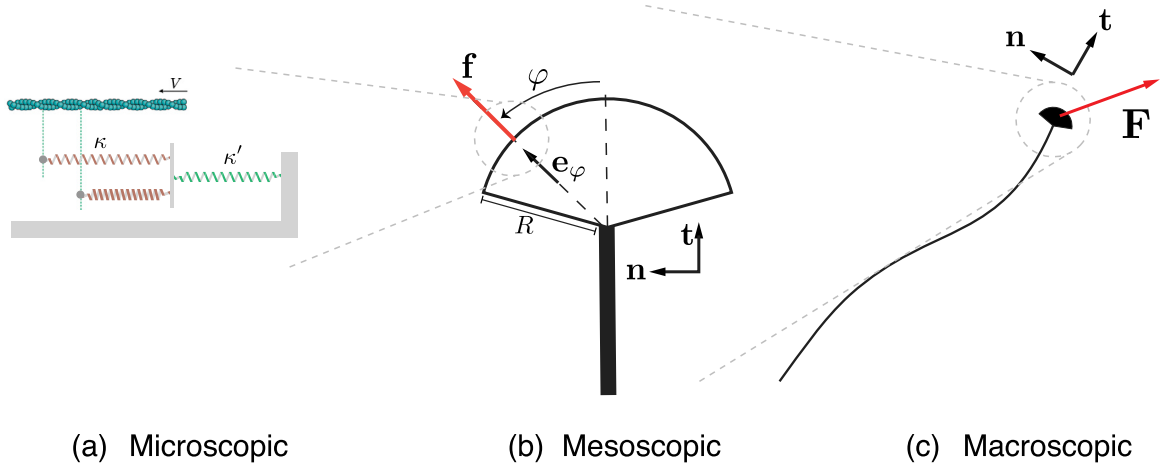


Fig. 2. General structure of the model. From left to right: microscopic scale—an actin filament is modelled as a rigid rod moving with velocity V w.r.t. the substrate. The filament is connected to the substrate through an evolving collection of springs modelling adhesive cross-linkers and the deformable substrate; mesoscopic scale—the growth cone is viewed as a continuous distribution of centripetally-aligned actin filaments with individual traction forces summing up to generate global net force on the axonal shaft; macroscopic scale—the axon is modelled as a morphoelastic filament subject to frictional forces between the shaft and the substrate and growth-cone-induced locomotory force.

2. The microscopic model

2.1. Adhesion of one actin filament

The mechanical interaction between the substrate and the cytoskeleton is mediated by adhesion proteins, henceforth generically termed *cross-linkers*. In the growth cone, tension in the substrate is generated by the movement of actin which stretches these cross-linkers. This tension opposes the retrograde motion of actin and pulls on the substrate, resulting reciprocally in a reaction force acting upon the axon shaft. The cross-linkers randomly bind and unbind, with a rate of unbinding that depends on their level of tension (Bell et al., 1984; Chan and Odde, 2008). Overall, random detachment and attachment of cross-linkers, combined with stretch-induced tension result in emergent frictional interactions between the actin and the substrate which depends on substrate stiffness (Chan and Odde, 2008; Sens, 2013). The emergence of this frictional force is the central mechanism considered here underlying growth cone locomotion.

To model the mechanical interaction between a single actin filament and the substrate, we adapt the approach of Sens (2013). The filament is modelled as a straight, infinite rigid rod moving relative to the substrate with velocity V , as shown in Fig. 3 (we also introduce the longitudinal position $X = Vt$, with t denoting the time coordinate). In the steady regime studied here, V is constant in time. We model the cross-linkers as linearly-elastic springs connecting the actin filament to the substrate. Each spring has an individual tension f , elongation x , and spring constant κ related through Hooke's law by

$$f = \kappa x. \quad (1)$$

The cross-linker tension can be related to the time Δt elapsed since its attachment. Indeed, for a perfectly rigid substrate, the tension of a single cross-linker since attachment is $f \approx \kappa V \Delta t$ (assuming that cross-linkers form unstretched, and neglecting the geometric nonlinearity due to the distance between the actin filament and the substrate). The situation is more complex in the case of a deformable substrate, where the cross-linkers may interact indirectly and non-locally with one another through short- and long-range deformations of the substrate (Nicolas et al., 2008). This deformation may be expressed in terms of the Green solution for an infinite half-plane subject to surface traction (Hwu, 2010; Sens, 2013).

Here, for simplicity, we assume that the substrate is soft so that cross-linkers interact mechanically as the substrate deforms almost uniformly. The substrate is then modelled as a single spring κ' with which all cross-linkers are connected in parallel. To model the kinetics of cross-linker detachment, we posit a Bell-type law (Bell, 1978), i.e. we assume that the probability that a cross-linker detaches in a small time-interval Δt is related to its tension f according to

$$p_{\text{off}} = k_{\text{off}} \Delta t e^{f/f_0}, \quad (2)$$

where f_0 is the characteristic force scale of detachment and k_{off} is the kinetic off-rate at rest. Further, we assume that cross-linkers form in the unstretched state at a constant rate k_{on} , so the probability of attachment during Δt is

$$p_{\text{on}} = k_{\text{on}} \Delta t. \quad (3)$$

Finally, we focus on a small section of the filament at the growth cone edge. Therefore, we assume that all material parameters are constant in space, which reduces the problem effectively to a zero-dimensional problem.

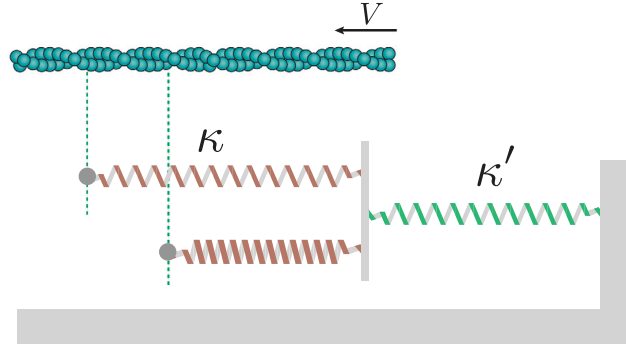


Fig. 3. Structure of the microscopic model. The actin filament moves with constant velocity V parallel to the substrate. We assume that all cross-linkers (brown springs with constant κ) interact with the same substrate spring (green spring with constant κ').

2.1.1. Mean-field treatment

The dynamics of focal adhesions has been previously analysed using continuum or computational approaches (e.g. Srinivasan and Walcott, 2009; Sabass and Schwarz, 2010; Bressloff, 2020), in particular with a focus on the role of substrate compliance in Chan and Odde (2008), Bangasser and Odde (2013) and Sens (2013). Similar to the mean-field approaches of Bangasser and Odde (2013) and Sens (2013) we here adopt a continuum perspective where we view the set of bound cross-linkers and their respective mechanical state as a continuum quantity. That is, we first consider the distribution of the extensions of bound cross-linkers. Let ρ be the density of bound cross-linkers per extension level, such that, at time t there are (on average) $dN = \rho(x, t) dx$ bound cross-linkers with extension in the infinitesimal interval $[x, x + dx]$. This density obeys the Lacker–Peskin equation (Srinivasan and Walcott, 2009)

$$\frac{\partial \rho}{\partial t} + v(x, t) \frac{\partial \rho}{\partial x} = B(x, t) - U(x, t), \quad (4)$$

where $B(x, t)$ and $U(x, t)$ denote, respectively, the kinetic binding and unbinding rates for cross-linkers at extension x ; and $v(x, t)$ is the extension rate of bound cross-linkers. Assuming a large, constant pool of free (unbound) cross-linkers with concentration c_{free} , binding occurs at constant rate $s_0 = \mathcal{V} k_{\text{on}} c_{\text{free}}$ (with unit inverse time), with \mathcal{V} the typical volume where binding reactions take place. Assuming that cross-linkers attach with zero extension, we posit an attachment rate of the form

$$B(x, t) = s_0 \delta(x), \quad (5)$$

with δ denoting the Dirac delta function. The Bell-type law for cross-linker detachment can be expressed as (Sens, 2013)

$$U(x, t) = k_{\text{off}} e^{\kappa x / f_0} \rho(x, t). \quad (6)$$

The extensions x and x_s of a cross-linker and the substrate, respectively, obey the virtual kinematic relation

$$\delta x + \delta x_s - \delta X = 0, \quad (7)$$

where δx , δx_s and δX denote virtual displacements of the cross-linker, the substrate and the actin filament, respectively.

Since we assumed previously that all cross-linkers are connected to the same substrate spring (κ'), the force balance is

$$\kappa' x_s = \int_0^\infty \kappa x \rho(x) dx. \quad (8)$$

In a virtual displacement of the filament we have

$$\kappa' \delta x_s = \int_0^\infty \kappa \delta x \rho(x) dx \quad (9)$$

(the density ρ is unaffected in a virtual displacement). Using (7) to remove δx_s we obtain

$$\chi (V \delta t - \delta x) = N \delta x, \quad (10)$$

where $\chi := \kappa' / \kappa$ is a dimensionless measure of the substrate stiffness; and where the total amount of bound cross-linkers is

$$N(t) = \int_0^\infty \rho(x, t) dx. \quad (11)$$

Since $v \delta t = \delta x$, we obtain

$$v = \frac{V}{1 + N / \chi}, \quad (12)$$

and we can rewrite the governing equation for ρ , (4), as

$$\frac{\partial \rho}{\partial t} + \frac{V}{1 + N / \chi} \frac{\partial \rho}{\partial x} = s_0 \delta(x) - k_{\text{off}} e^{\kappa x / f_0} \rho(x, t). \quad (13)$$

2.1.2. Steady-state traction

Henceforth, we restrict our attention to time-independent solutions of the problem so we set $\partial\varrho/\partial t = 0$ in (13). The total force T exerted by the cross-linkers on the actin filament is

$$T = \int_0^\infty \kappa x \varrho(x) dx, \quad (14)$$

which, after integration of (13), yields

$$T(\chi, \nu) = f_0 K \mathcal{H} \left(\frac{q}{\chi \nu} (\chi + N) \right). \quad (15)$$

Here the dimensionless parameters $K := s_0/k_{\text{off}}$, $q := f_0/\kappa\ell$ and $\nu := V/k_{\text{off}}\ell$ denote respectively the binding constant of cross-linkers, their bond strength, and a dimensionless measure of actin velocity (with ℓ the arbitrary typical extension length of cross-linkers); and \mathcal{H} is the special function defined as

$$\mathcal{H}(r) := r e^r \int_0^\infty y \exp(-r e^y) dy, \quad r > 0. \quad (16)$$

The total number of cross-linkers, N , defined in (11) and present in (15), satisfies at steady state the equation

$$N = \frac{K}{\nu} \int_0^\infty \exp \left[\frac{q(\chi + N)}{\chi \nu} \left(1 - \exp \left(-\frac{\chi y}{q(\chi + N)} \right) \right) \right] dy. \quad (17)$$

2.1.3. Force balance

We have derived in (15) and (17) a relation linking traction generation with actin velocity and substrate stiffness. However, the motion of actin itself results from the activity of myosin motors at the rear of the growth cone, thus, the dimensionless velocity ν is not prescribed, but is instead an unknown that is obtained from the force balance between actin and the myosin motors.

The forces acting on a single actin filament are generated by myosin contraction (Lin et al., 1996) modelled as a constant force M . In addition, actin is subject to viscous friction with the cytoplasm (with constant Ξ), as well as the traction force generated by the cross-linkers, $T(\chi, \nu)$ given by (15). Thus, neglecting inertial effects, the force balance reads

$$M - T(\chi, \nu) - \Xi V = 0. \quad (18)$$

We define $u := q(1 + \chi^{-1}N)/\nu$ and $\xi := k_{\text{off}}\Xi f_0/\kappa$, to remove the dependence upon ν from (17) and (18):

$$\chi (M - f_0 K \mathcal{H}(u)) u - \xi (\chi + N) = 0, \quad (19a)$$

$$N = \frac{K u \chi}{q(\chi + N)} \int_0^\infty \exp \left[u \left(1 - \exp \left(-\frac{\chi y}{q(\chi + N)} \right) \right) \right] dy, \quad (19b)$$

where we have used (12). For a given χ , (19) forms a system of equations for the unknowns (u, N) . The solution to that system can be substituted into (15) to obtain the traction

$$T(\chi) = f_0 K \mathcal{H}(u), \quad (20)$$

where u is viewed as an implicit function of χ . This expression relates the traction force to the substrate stiffness directly, in contrast to the work of Sens (2013) where the traction force is obtained for a given actin velocity ν .

2.2. Optimal stiffness

As can be seen, for a range of parameters, the traction-stiffness function $T(\chi)$ may exhibit global maximum at a stiffness χ^* . We call χ^* the *optimal stiffness* defined as the (dimensionless) stiffness where traction is maximal $T_{\text{max}} = T(\chi)$. At that value, the ability of the axon to develop traction forces on the substrate is maximal. From (20) we see that $T(\chi)$ is maximal when $\mathcal{H}(u(\chi))$ is maximal. The function $\mathcal{H}(r)$ has a global maximum at $r = r^* \approx 0.387$ (at which point $\mathcal{H}(r^*) \approx 0.298$), and therefore $T(\chi)$ is maximised when $u(\chi) = r^*$.

Substituting $u = r^*$ and $N = N^*$ into (19) and rearranging the terms, we obtain

$$\chi^* = \frac{\xi N^*}{r^* (M - f_0 K \mathcal{H}(r^*)) - \xi}, \quad (21a)$$

$$N^* = \frac{K r^* \chi^*}{q(\chi^* + N^*)} \int_0^\infty \exp \left[r^* \left(1 - \exp \left(-\frac{\chi^* y}{q(\chi^* + N^*)} \right) \right) \right] dy. \quad (21b)$$

This defines a system of two equations for the two unknowns (χ^*, N^*) . Remarkably, there exists a closed-form solution for this system given by

$$\chi^* = \frac{\xi K r^* e^{r^*} \Gamma(0, r^*)}{r^* (M - f_0 K \mathcal{H}(r^*)) - \xi}, \quad N^* = K r^* e^{r^*} \Gamma(0, r^*), \quad (22)$$

with $\Gamma(s, x)$ the upper incomplete gamma function.

Since N^* is positive if χ^* is positive, we see from (22) that the condition for the existence of a positive local maximum χ^* is

$$r^* (M - f_0 K H(r^*)) - \xi > 0. \quad (23)$$

When this condition is not satisfied, the traction is a strictly increasing function of χ with a horizontal asymptote at $\chi \rightarrow \infty$. Importantly, we will show in Section 3 that the emergence of negative durotaxis is directly predicated upon the existence of a positive optimal stiffness via the condition (23). Moreover, the second derivative $T''(\chi^*)$ of the traction $T(\chi)$ at the optimal stiffness χ^* characterises the behaviour of the system near this optimum. Differentiating (20) twice w.r.t. χ and setting $\chi = \chi^*$ we obtain

$$T''(\chi^*) = f_0 K H''(r^*) u'(\chi^*)^2. \quad (24)$$

An exact expression for $u'(\chi^*)$ in the previous equation is obtained by differentiating (19) w.r.t. χ at $\chi = \chi^*$, providing a system of two equations for the unknowns $u'(\chi^*)$ and $N'(\chi^*)$, which can be solved to obtain

$$u'(\chi^*) = \left[1 + \frac{1}{r^*} \left(\frac{e^{r^*}}{\text{Chi}(r^*) - \text{Shi}(r^*)} + \frac{k_{\text{off}} \Xi}{k_{\text{off}} \Xi + r^* (K K H(r^*) - M K / f_0)} \right) \right]^{-1}, \quad (25)$$

with Chi and Shi the hyperbolic cosine and sine integrals, respectively.

2.3. The effect of myosin contractility

The parameter M quantifies the force of myosin contraction, which plays an important role in axon guidance (McCormick and Gupton, 2020; Turney and Bridgman, 2005). The parameter M changes qualitatively the traction-stiffness curve. Indeed, we define M_{crit} the value of M at which the inequality (23) is an equality, that is,

$$M_{\text{crit}} \stackrel{\text{def}}{=} f_0 K H(r^*) + \xi / r^*. \quad (26)$$

This critical force defines two distinct behaviours.

First, for $M > M_{\text{crit}}$, when myosin contraction is sufficiently large, as shown in Fig. 4, there exists an optimal stiffness and the behaviour of the system is controlled by three important features of the traction-stiffness curve: (i) the optimal stiffness χ^* ; (ii) the curvature $T''(\chi^*)$ defining how quickly traction changes close to the optimal stiffness; (iii) the asymptotic traction generated on a rigid substrate $T_\infty := \lim_{\chi \rightarrow \infty} T(\chi)$. We note that the optimal stiffness χ^* is a decreasing function of M and tends to zero as $M \rightarrow \infty$; see (22). As can be seen from (24) and (25), $T''(\chi^*)$ is a bounded, increasing function of M such that

$$T''(\chi^*) \xrightarrow{M \rightarrow \infty} f_0 K H''(r^*) \left(1 - \frac{e^{-r^*}}{r^* \Gamma(0, r^*)} \right)^{-2} \quad (27)$$

This asymptotic value is the maximal curvature achievable at χ^* by modulating contractility M . We see that the curvature increases as $\chi^* \rightarrow 0$ as $M \rightarrow \infty$. However, there is a physical bound to the value of M depending on available binding sites. This relationship shows that the larger the myosin contraction, the faster an axon will react to changes in stiffness close to the optimal stiffness.

To investigate the behaviour of T_∞ in the limit $M \rightarrow \infty$, we first divide (19a) by χ and take the limit $\chi \rightarrow \infty$ to obtain

$$u(M - f_0 K H(u)) - \xi = 0. \quad (28)$$

Note that $T_\infty = f_0 K H(u)$ in the above equation and therefore we are concerned with the asymptotics of $H(u)$ in the limit $M \rightarrow \infty$. Showing that $u \sim \xi/M$ as $M \rightarrow \infty$, it follows that $T_\infty \sim f_0 K H(\xi/M) \rightarrow 0$.

Second, when myosin contraction is weak, that is for $M < M_{\text{crit}}$, there is no maximum and traction is a monotonically increasing function of χ , plateauing to $T_\infty = \lim_{\chi \rightarrow \infty} T(\chi)$. Noting that $u \sim (\xi + f_0 K) / M$ as $M \rightarrow 0$ we obtain

$$T_\infty \underset{M \rightarrow 0}{\sim} f_0 K H\left(\frac{\xi + f_0 K}{M}\right) \sim \frac{f_0 K M}{\xi + f_0 K}. \quad (29)$$

We see that as M increase past M_{crit} , T_∞ decreases. Hence, for large myosin contraction, axons growing on a very rigid substrate will exert a reduced traction.

3. The mesoscopic model

Macroscopically, the total force generated by the growth cone results from the centripetal flow of all actin filaments organised radially in the lamellipodium towards the growth cone base. We assume that the specific shape of the growth cone has little effect on the net force generated by the cone. Hence we model it as a circular sector with central angle $2\varphi_0$ and radius R ; see Fig. 2. Here, we denote by \mathbf{r} the position of the base of the growth cone in the laboratory frame equipped with the canonical basis $\{\mathbf{e}_x, \mathbf{e}_y\}$. We denote by \mathbf{t} the unit vector along the axis of symmetry of the growth cone that is also the tangent to the axon attached to the growth cone, and \mathbf{t}^\perp the normal unit vector to \mathbf{t} . We define $\mathbf{e}_\varphi = \cos \varphi \mathbf{t} + \sin \varphi \mathbf{t}^\perp$, with $\varphi \in [-\varphi_0, \varphi_0]$, the unit vector pointing outward in the direction φ .

The force density applied at the edge of the disk along the direction φ depends on the local substrate stiffness at the lamellipodium edge at this location, i.e. at the point $\mathbf{r} + R\mathbf{e}_\varphi$. Neglecting the mutual mechanical interactions between the filaments, the resultant force applied at the distal end of the axon shaft is given by

$$\mathbf{F}(\mathbf{r}, \mathbf{t}) = \int_{-\varphi_0}^{\varphi_0} \rho T(\chi(\mathbf{r} + R\mathbf{e}_\varphi)) \mathbf{e}_\varphi R d\varphi. \quad (30)$$

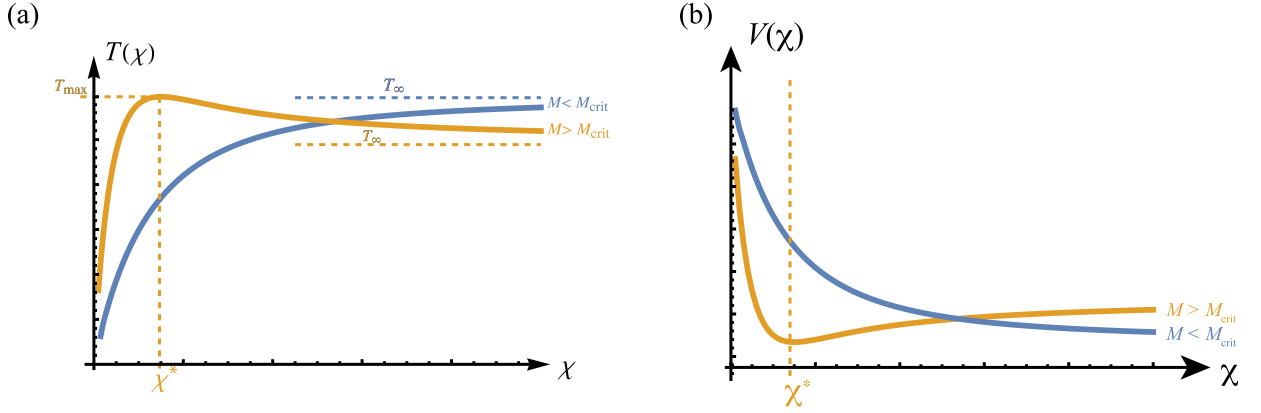


Fig. 4. (a) Profile of the traction-stiffness curve $T(\chi)$. For small myosin concentration, $M < M_{\text{crit}}$, the traction increases monotonically as a function of the stiffness. For large myosin concentration, $M > M_{\text{crit}}$, traction has a maximum value at the optimal stiffness χ^* . (b) Profile of actin speed as a function of stiffness. For small myosin concentration, $M < M_{\text{crit}}$, the speed decreases monotonically as a function of the stiffness. For large myosin concentration, $M > M_{\text{crit}}$, actin speed has a minimum value at the optimal stiffness χ^* .

with ρ the density of adhesion sites per unit arclength along the growth cone edge (which we assume to be constant); and where $T(\chi)$ is the individual filament force given by (20) evaluated at the edge of the growth cone where adhesion sites are located. Note that, since all the filaments point towards the base of the growth cone, there is no induced torque about that point, thus changes in direction may only be induced through an asymmetric distribution of forces across the growth cone. The expression (30) is difficult to work with as it implies evaluating T for every φ . To make progress, we assume that the stiffness field varies slowly in the vicinity of the growth cone – equivalently that the growth cone is small – so we expand (30) to $O(R^2)$ to obtain

$$\mathbf{F}(\mathbf{r}, t) = 2R\rho \sin \varphi_0 T(\chi) \mathbf{t} + R^2 \rho \varphi_0 T'(\chi) \mathbf{P}(\varphi_0) \nabla \chi + O(R^3). \quad (31)$$

where χ and $\nabla \chi$ are evaluated at \mathbf{r} ; and where the tensor \mathbf{P} reflects the geometry of the growth cone only and is given by

$$\mathbf{P}(\varphi_0) := \int_{-\varphi_0}^{\varphi_0} \mathbf{e}_\varphi \otimes \mathbf{e}_\varphi \frac{d\varphi}{\varphi_0} = \mathbf{1} + \frac{\sin 2\varphi_0}{2\varphi_0} (\mathbf{t} \otimes \mathbf{t} - \mathbf{t}^\perp \otimes \mathbf{t}^\perp), \quad (32)$$

Here, $\mathbf{1}$ is the identity tensor, and ‘ \otimes ’ denotes the tensor product (i.e. given vectors \mathbf{u} and \mathbf{v} , the Cartesian components of $\mathbf{u} \otimes \mathbf{v}$ are $(\mathbf{u} \otimes \mathbf{v})_{ij} = u_i v_j$). From this expansion, the role of substrate stiffness and its gradient can be interpreted physically.

The first term on the r.h.s. of (31) is a stiffness-dependent force component in the current direction of the axon, regulating the longitudinal growth velocity. The second term captures the durotactic effect induced by a gradient in substrate stiffness $\nabla \chi$, which will cause the axon to steer away or towards stiffness gradients. In the special cases $\varphi_0 = \pi/2$ (half-disk) or $\varphi_0 = \pi$ (full disk), the durotactic component is aligned with $\nabla \chi$ as $\mathbf{P}(\pi) = \mathbf{P}(\pi/2) = \mathbf{1}$. More in general, the durotactic force component is not aligned with $\nabla \chi$ as $\nabla \chi \times \mathbf{P} \nabla \chi \neq \mathbf{0}$. However, since \mathbf{P} is symmetric positive, we have that $\nabla \chi \cdot (\mathbf{P} \nabla \chi) \geq 0$, thus, if $T'(\chi) > 0$, the durotactic force makes an acute angle with the stiffness gradient. Consequently, the orientation of the durotactic force, that is, whether the axon progresses towards soft or stiff substrate, is only governed by the sign of $T'(\chi)$. We have *positive durotaxis* if $T'(\chi) > 0$ and *negative durotaxis* if $T'(\chi) < 0$. Note that, as expected, the normal component of the durotactic force vanishes when the axon is aligned with the gradient.

From (31), we can directly obtain the factors determining the strength of the durotactic force. We define the dimensionless *durotactic sensitivity* as

$$\vartheta(\chi) = \frac{\varphi_0}{\sin \varphi_0} \frac{T'(\chi)}{T(\chi)}, \quad (33)$$

measuring the relative effect of the deflective force to the longitudinal traction. From Section 2, it follows that ϑ vanishes at the optimal stiffness χ^* , the stationary point of T . For $\chi < \chi^*$, we have $\vartheta > 0$ and, conversely, $\vartheta < 0$ for $\chi > \chi^*$.

From the mesoscopic model, we conclude that: *Axons growing on substrates with stiffness smaller than the optimal stiffness χ^* can only exhibit positive durotaxis; conversely, axons on substrates stiffer than the optimal stiffness can only exhibit negative durotaxis.* In particular, if condition (23) is violated, axons can only undergo positive durotaxis.

4. The macroscopic model

In the previous two sections, we have derived the overall net force applied to the tip of the growing axon due to the interaction of the growth cone with the substrate. We can now use this force and model the axon as a morphoelastic rod, i.e. a growing elastic rod (see Chap. 5 and 6 of Goriely, 2017) subject to the end loading due to the growth cone and to the frictional force exerted by the substrate, thus generalising the approach of O’Toole et al. (2008) to curved trajectories.

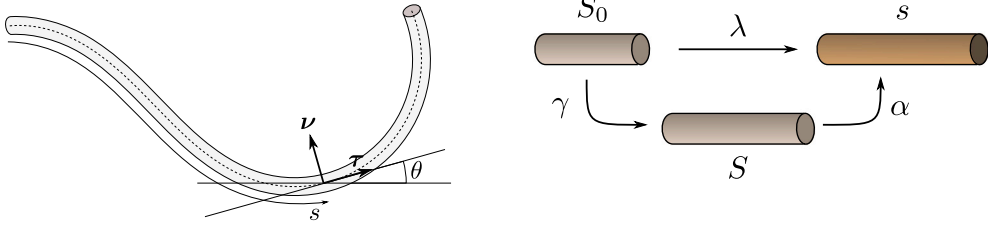


Fig. 5. A morphoelastic rod model. Left: At a point s in the current configuration, we defined the tangent vector τ and normal vector τ^\perp through the angle θ . Right: In the growth model we assume that a infinitesimal element of the rod located initially at S_0 is subject to both a growth deformation γ and an elastic deformation α , such that the total stretch is $\lambda = \alpha\gamma$.

4.1. Morphoelastic rod model

Initially, a morphoelastic rod is defined by a smooth curve $\mathbf{R}_0(S_0) = (X_0(S_0), Y_0(S_0)) \in \mathbb{R}^2$ with arclength $S_0 \in [0, L_0]$. We choose $S_0 = 0$ to be at the base (the soma) and $S_0 = L_0$ at the axon tip (growth cone). As the axon grows and deforms elastically under loads, the rod adopts a new *current* configuration parameterised by the material coordinate S_0 and time t by $\mathbf{r}(S_0, t) = (x(S_0, t), y(S_0, t))$. We define $s(S_0, t)$ the arclength in the current configuration, i.e. the contour length between the base and the material point that was at position S_0 and time $t = 0$. The Frenet–Serret frame of the current curve is composed of the unit tangent vector $\tau = \partial \mathbf{r} / \partial s$ (pointing towards the growth cone) and the unit normal vector τ^\perp , perpendicular to τ . Both can be encoded by a single angle θ between the x -axis and the tangent vector so that

$$\tau = (\cos \theta, \sin \theta), \quad \tau^\perp = (-\sin \theta, \cos \theta). \quad (34)$$

At the tip, the orientation of the axon agrees with that of the growth cone so that $\tau(L_0) = \mathbf{t}$ and $\tau^\perp(L_0) = \mathbf{t}^\perp$. Then the Frenet–Serret equations can be written as

$$\frac{\partial x}{\partial S_0} = \lambda \cos \theta, \quad \frac{\partial y}{\partial S_0} = \lambda \sin \theta, \quad \frac{\partial \theta}{\partial S_0} = \lambda k, \quad \lambda = \frac{\partial s}{\partial S_0}, \quad (35)$$

where λ is the stretch and k the signed curvature. The pair of scalar fields (λ, k) then fully describes the geometry of the rod (stretching and bending) (see Fig. 5).

Neglecting inertial effects and body torques, the balance of linear and angular momenta is expressed in terms of the internal resultant force $\mathbf{n} = (n_x, n_y)$ and moment m applied by a cross-section S_0^+ onto a cross-section S_0^- as (see chapter 5 of Goriely, 2017, for details)

$$n'_x + \lambda b_x = 0, \quad (36a)$$

$$n'_y + \lambda b_y = 0, \quad (36b)$$

$$m' + n_y \cos \theta - n_x \sin \theta = 0, \quad (36c)$$

where the apostrophe denoting differentiation w.r.t. S_0 ; and $\mathbf{b} = (b_x, b_y)$ is a density of body force per unit current length, that is used to model the adhesion between the growing shaft and the substrate as a linear frictional force with coefficient ζ (O'Toole et al., 2008; Oliveri et al., 2021; Oliveri and Goriely, 2022)

$$\mathbf{b} = -\zeta \tau. \quad (37)$$

Here the overdot denotes the material derivative, linked to the Eulerian derivative through the formula $\dot{\mathbf{r}} - \dot{s}\tau = \partial \mathbf{r}(s, t) / \partial t$.

To close the system, we must formulate constitutive relationships that relate stresses to deformations. We assume that the rod is extensible but unshearable. In a growing rod, only part of the deformation results in stresses, reflecting the remodelling and growth of the material and the resulting change in reference configuration. To model this effect, we introduce an intermediate reference configuration $\mathbf{R}(S_0, t)$ with arclength $S(S_0, t)$, representing the equilibrium configuration of the rod achieved upon removal of the loads. We decompose the total deformation multiplicatively, in terms of the elastic, and growth stretches, respectively $\alpha := \partial s / \partial S$ and $\gamma := \partial S / \partial S_0$ (Goriely, 2017):

$$\lambda = \alpha\gamma \quad (38)$$

(see Fig. 5). Constitutively, we assume that only α and k generate stresses. Therefore, we posit a quadratic elastic energy density (energy per unit intermediate length) for a morphoelastic rod with intrinsic curvature \hat{k} , of the form

$$W(\alpha, k) = \frac{1}{2} \mathcal{K}(\alpha - 1)^2 + \frac{1}{2} \mathcal{B}(k - \hat{k})^2, \quad (39)$$

where \mathcal{K} and \mathcal{B} are the extensional and bending stiffnesses, respectively. The corresponding constitutive relations are

$$n = \frac{\partial W}{\partial \alpha} = \mathcal{K}(\alpha - 1), \quad (40a)$$

$$m = \frac{\partial W}{\partial k} = B(k - \hat{k}), \quad (40b)$$

with $n := \mathbf{n} \cdot \boldsymbol{\tau} = n_x \cos \theta + n_y \sin \theta$, the longitudinal tension.

There are two remaining important components to model, the growth of the axonal shaft specified by γ , and the remodelling of the curvature \hat{k} . Physically, growth is due to mechanical stresses along the shaft that cause the axon to creep irreversibly above some critical tension (Franze and Guck, 2010; Suter and Miller, 2011; Goriely et al., 2015), while new cytoplasmic material is incorporated simultaneously into the shaft (O'Toole and Miller, 2011). During this process, cross-sectional area remains mostly constant, indicating that the cell maintains a homeostatic density (Dennerll et al., 1989; Lamoureux et al., 1989); thus we assume that \mathcal{K} and B are constant in time and uniform along the rod. To model diffuse growth at each point, we use the exponential growth law (Oliveri and Goriely, 2022)

$$\frac{1}{\gamma} \frac{\partial \gamma}{\partial t} = \frac{(n - n_0)_+}{\eta}, \quad (41)$$

where $(n - n_0)_+ = n - n_0$ for $n \geq n_0$ (0 otherwise); $n_0 \geq 0$ is the *critical tension* below which no growth occurs; and η plays the role of a morphoelastic viscosity (in unit force times time). Henceforth, for simplicity, we neglect the threshold effect and we set $n_0 = 0$.

We also assume a relaxation process for the bending moment due to internal remodelling by using the curvature evolution law

$$\dot{\hat{k}} = \frac{k - \hat{k}}{\tau_k}, \quad (42)$$

with a characteristic timescale τ_k of the same order as η/n_0 .

The connection to the mesoscopic model is obtained through the boundary conditions. At the base $S_0 = 0$, the rod is clamped

$$\mathbf{r}(0) = \mathbf{r}_0, \quad \theta(0) = \theta_0, \quad (43)$$

where \mathbf{r}_0 and θ_0 are the base position and angle. At its tip, the rod is subject to the traction exerted by the growth cone:

$$m(L_0) = 0, \quad \mathbf{n}(L_0) = \mathbf{F}(\mathbf{r}(L_0), \theta(L_0)), \quad (44)$$

where \mathbf{F} depends on the growth cone position and orientation through the mesoscopic law (31).

There are three important parameters in the problem, the dimensionless parameter $\mathcal{Z} := B\zeta/\mathcal{K}\eta$, which measures the relative effect of adhesion w.r.t. viscosity, and the two characteristic lengths

$$\Lambda = \sqrt{\eta/\zeta}, \quad \mathcal{L} = \sqrt{B/F}. \quad (45)$$

The *growth length* Λ measures the distance over which axonal tension dissipates into the substrate due to friction (O'Toole et al., 2008; Oliveri et al., 2021; Oliveri and Goriely, 2022), and \mathcal{L} is the *bending length* that measures the typical curvature radius of a beam due to the typical transverse traction F from the growth cone.

At any time, given $\gamma(S_0, t)$ and $\hat{k}(S_0, t)$, the boundary-value problem formed by (35)–(38), (40) and (41) with the boundary conditions (43) and (44), can be solved numerically to obtain the axon's trajectory. However, the frictional interaction between the axon and its substrate dissipates traction forces over a region close to the growth cone which becomes short, relatively to the entire axon, as time progresses. Thus, only a short and essentially constant distal section of the axon is dynamic, rapidly causing important computational difficulties due to our Lagrangian specification of the problem. Rather than solving for the system directly, we can take advantage of this effect and focus our attention on the growth process localised in a distal region, and freeze the most proximal part of the axon to account for permanent adhesion between the axon and the substrate (and discard that frozen region from the problem). This process is described in the next section.

4.2. Tip growth approximation

The existence of a characteristic lengthscale Λ can be used to further simplify the problem. For axons, we have $\Lambda \ll \mathcal{L}$ as the force applied by the growth cone only creates small deflections (hence a large radius of curvature \mathcal{L}). This scaling has two important consequences.

First, the effect of the force applied at the tip of the axon by the growth cone on the rest of the axon vanishes quickly away from the tip. It implies that only a short zone at the tip of length L that is of order Λ is subject to a force. In terms of modelling, we exploit this result computationally by constraining the dynamic region of the axon to a moving active portion of fixed arclength L while segments of the axon found at a greater arclength are fixed and do not need to be updated. In morphoelasticity, this process is referred as *tip growth* (Goriely, 2017) and is found in plant shoots or roots, which undergo elongation over an effectively finite apical (or sub-apical) region (Silk and Erickson, 1979).

Second, since the active zone is small w.r.t. the typical radius of curvature, only small deflections away from the natural state take place in response to the growth cone. The distal end of the beam – the axon's tip – is subject to the locomotory force \mathbf{F} produced by the growth cone. The basal end makes the junction between the dynamic region and the frozen region, and is assumed to be clamped from the point of view of the elastic quasi-equilibrium. Therefore, we can approximate the shape of the active zone by

$$\mathbf{r}(\sigma, t) = \hat{\mathbf{r}}(t) + x(\sigma, t) \hat{\mathbf{t}}(t) + y(\sigma, t) \hat{\mathbf{v}}(t), \quad \sigma \in [0, L], \quad (46)$$

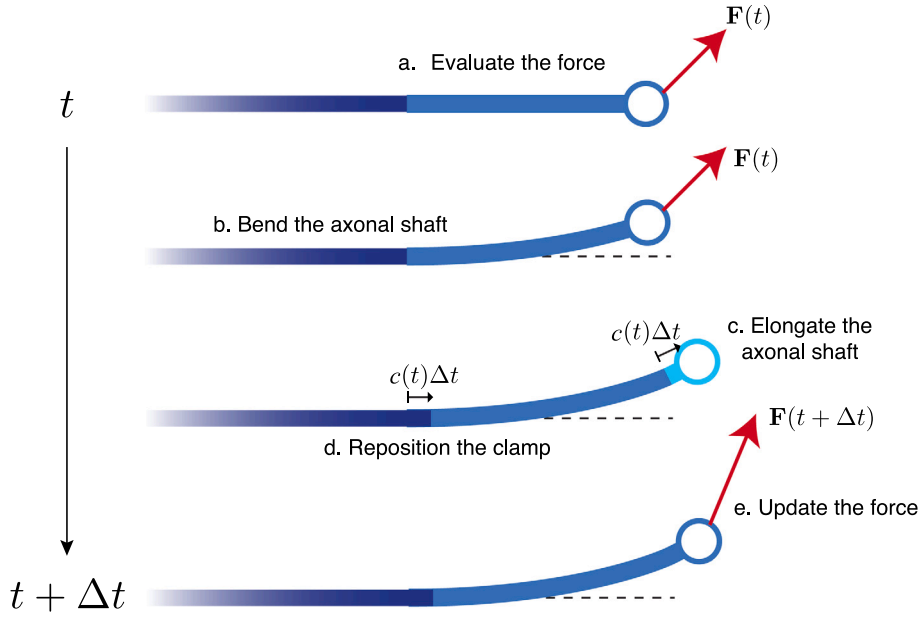


Fig. 6. Schematic of the incremental axonal growth process. We assume that only a segment of length L and clamp angle $\hat{\theta}$ is subject to bending and remodelling. When a force is applied, this clamped beam element bends. Once deformed it grows by an amount $c(t)\Delta t$ and the new clamp is moved and rotated to the new angle $\hat{\theta}(t)$.

where $\hat{r} = (\hat{x}, \hat{y})$ and $\hat{r}(t)$ is the position of the clamp; $\hat{\tau} = \cos \hat{\theta} \mathbf{e}_x + \sin \hat{\theta} \mathbf{e}_y$ and $\hat{\nu} = -\sin \hat{\theta} \mathbf{e}_x + \cos \hat{\theta} \mathbf{e}_y$ are the tangent and normal vectors to the curve at the base, with $\hat{\theta}$ the angle of the clamp to the horizontal \mathbf{e}_x (henceforth, we denote quantities evaluated at the base of the beam with a circumflex); x and y , typeset in the sans-serif font, denote the coordinates of the rod in the frame of the clamp. For small deflection we have $x(\sigma, t) \approx \sigma$, and the rod equations of the previous section simplify to the beam equations (Goriely, 2017, p. 147).

There is however an important subtlety appearing in the problem. Since the active zone is moving in time, we have to properly advect the position of the beam element as the axon grows. We keep track of the position and direction of the clamp through the position vector $\hat{r}(t)$ and model the evolution of $r(\sigma, t)$ as the limit in small time step Δt of the following process (Fig. 6): At t the beam is clamped at $\hat{r}(t)$ with direction $\hat{\tau}(t)$ and is subject to a distal load $F(t)$ and viscous friction along its length. First, $y(\sigma, t)$ evolves according to the linear beam equations for a time interval of length $\Delta t \ll 1$. Then, a linear segment of length $c(t)\Delta t$ is added to the end of the beam in the direction of the tip. We call $c(t)$ the growth rate of the axon. Finally, the length constraint is enforced by setting the new profile of the beam, $r(\sigma, t + \Delta t)$ to be the segment of length L from the tip of the grown, deflected beam profile.

Taking the limit $\Delta t \rightarrow 0$, we obtain the continuous-time evolution equations (see details in Appendix A):

$$\frac{\partial y}{\partial t} - c(t) \frac{\partial y}{\partial \sigma} = \frac{1}{\zeta} \left(\frac{\partial^2 y}{\partial \sigma^2} F \cdot \hat{\tau} - B \frac{\partial^4 y}{\partial \sigma^4} \right) - \sigma \hat{R}(t), \quad (47a)$$

$$\frac{\partial \hat{\theta}}{\partial t} = \hat{R}(t), \quad (47b)$$

$$\frac{\partial \hat{r}}{\partial t} = c(t) \hat{\tau}, \quad (47c)$$

$$\hat{R}(t) := c(t) \frac{\partial^2 y}{\partial \sigma^2}(0, t). \quad (47d)$$

The deflection $y(\sigma, t)$ satisfies the boundary conditions

$$y(0, t) = 0, \quad \frac{\partial y}{\partial \sigma}(0, t) = 0, \quad (48a)$$

$$\frac{\partial^2 y}{\partial \sigma^2}(L, t) = 0, \quad B \frac{\partial^3 y}{\partial \sigma^3}(L, t) - F \cdot \hat{\tau} \frac{\partial y}{\partial \sigma}(L, t) = -F \cdot \hat{\nu}. \quad (48b)$$

Conditions (48a) define a clamp at $\sigma = 0$, while (48b) enforces the load F applied with no torque on the beam at $\sigma = L$.

The growth speed c depends on the force exerted by the growth cone on the tip of the axon. Solving the system in the steady regime for rectilinear expansion (see O'Toole et al., 2008; Oliveri et al., 2021; Oliveri and Goriely, 2022), provides, for small deflection and to leading order, a growth velocity of the form

$$c = \frac{F \cdot \mathbf{t}}{\sqrt{\eta \zeta}}. \quad (49)$$

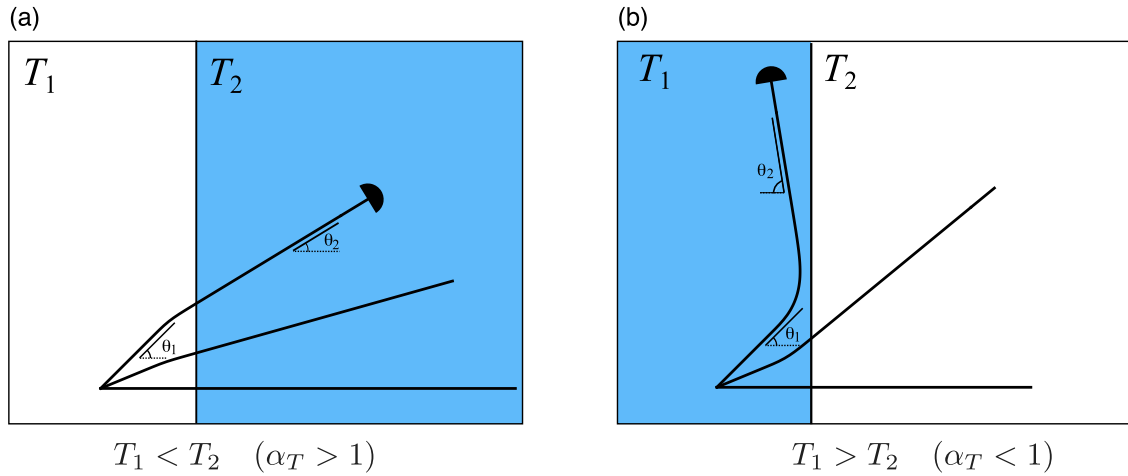


Fig. 7. Simulations of axons refracting across and reflecting against an interface with incidence angle θ_1 and reflection or refraction angle θ_2 . (a) When the traction exerted by the growth cone is smaller on the right substrate (here $\alpha_T = 5/4$), the axon can only refract. (b) When the traction exerted by the growth cone is larger on the right substrate (here $\alpha_T = 4/5$), the axon can reflect or refract depending on the incidence angle. Parameters in both scenarios: $\lambda = R/4$, $R = L/2$, $\varphi_0 = \pi/2$, $\beta = 0.05$.

We have developed a minimal model with two main components. From the microscopic model we have a mapping from substrate rigidity to the traction exerted by the growth cone, and from the mesoscopic model we obtain the shape of the axon as a function of time by locally integrating a clamped beam equation and advecting the clamp accordingly (our numerical method is described in [Appendix B](#)). We are now in a position to use this model to understand the effects of varying substrate rigidity on the motion and shape of axons.

5. Axonal optics: reflection, refraction and focalisation of axons

In this section, we explore canonical properties of our theory emerging from the interaction between the axon and a substrate with heterogeneous rigidity. More specifically, we examine two key cases: a straight interface between two regions of uniform stiffness; and a graded field of stiffness defined by a uniform gradient. The question then is to identify the essential laws that govern the motion of an axon within such fields.

5.1. Reflection and refraction at a straight stiffness interface

We consider a heterogeneous field composed of two regions with different but uniform stiffnesses separated by a straight interface. In this case, the axon can either grow through the interface (refraction) or bounce against the interface (reflection), in analogy with optic ray theory ([Oliveri et al., 2021](#)). As the growth cone touches the interface, the force density along the growth cone margin becomes heterogeneous.

We assume that the axon grows from the region $x < 0$, as shown in [Fig. 7\(a\)](#), and approaches the boundary with an angle of incidence $\theta_1 \in [0, \pi/2)$ (the angle between the axon and the normal to the interface). We assume that the interface is sharp but numerically, we approximate this straight interface by

$$T(x, y) = \frac{T_1 + T_2}{2} + \frac{T_2 - T_1}{2} \tanh(x/\lambda), \quad (50)$$

where $T_1 = T(\chi_1)$ and $T_2 = T(\chi_2)$ are the force densities produced by the growth cone in the left-most and right-most regions, which depend on the stiffness of each region (χ_1, χ_2). The parameter λ determines the length scale of the transition from T_1 to T_2 across the interface and is chosen small enough w.r.t. the growth cone size, such that further reduction does not affect the results. (in practice, we found that $\lambda = R/4$ is suitable). The total force depends nonlinearly on the position and orientation of the growth cone via (30), since, here, the large steepness of the gradient $\sim (T_2 - T_1)/2\lambda$ precludes the use of the leading-order approximation (31).

Initially, we assume a clamp position $\mathbf{r}_0(0)$ far from the interface in the incidence direction θ_1 . After the growth cone crosses the interface region, it follows a straight trajectory which defines the *refraction angle* θ_2 w.r.t. the normal pointing into the right region. The axon may also reflect against the interface and stay in the left-most region as seen in [Fig. 7\(b\)](#). In this case, the *reflection angle* θ_2 is defined as the angle between the left normal and the direction of the axon. Let $\theta_m = \lim_{t \rightarrow \infty} \theta_0(t) \bmod 2\pi$, then restricting our attention to $\theta_m \in [0, \pi)$ we have

$$\theta_2 = \begin{cases} \theta_m, & \text{if } 0 \leq \theta_m < \pi/2, \\ \pi - \theta_m, & \text{if } \pi/2 \leq \theta_m < \pi. \end{cases} \quad (51)$$

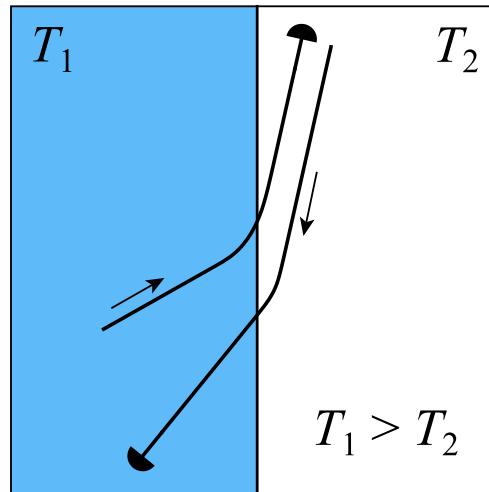


Fig. 8. Demonstration of the absence of time-reversibility in the system. Approaching the interface from the left is not the same as approaching from the right. An axon travelling from blue to white with an angle w.r.t the vertical θ_1 ends with an angle θ_2 . The same axon travelling from white to blue with an angle θ_2 will end with a direction given by $\tilde{\theta}_1 \neq \theta_1$. Parameters: $R = L/2$, $\lambda = R/4$, $\varphi_0 = \pi/2$, $\alpha_T = 4/5$, $\beta = 0.05$.

By choosing the characteristic force-scale of the system to be $2R\rho T_1 \sin \varphi_0$, which is equal to the magnitude of the total growth cone force when $\chi = \chi_1$, we obtain the two dimensionless parameters

$$\alpha_T := \frac{T_2}{T_1}, \quad \beta := \frac{B \csc \varphi_0}{2R\rho T_1 L^2}. \quad (52)$$

In particular, β relates to the typical radius of curvature of the axon, that is, smaller β generates larger deflections. A physiological range can be estimated for the value of β . The bending stiffness of the axon, B , is estimated to be between 5×10^{-22} N m² and 6×10^{-19} N m² (Lang et al., 2017). The growth cones of axons of different types of neurons can generate net traction forces of varying magnitudes. These traction forces, equal to $2R\rho T_1 \sin \varphi_0$, can range from 0.1 nN to 2 nN (Koch et al., 2012). Finally, the length of the beam, L , is on the order of $\Lambda = \sqrt{\eta/\zeta}$. We assume that $L = \Lambda$ and estimate $\Lambda \approx 32$ μ m using the estimates $\eta \approx 10^{-5}$ Ns, $\zeta \approx 10^4$ Pa.s from O'Toole et al. (2008). Combining all of these estimates together, we conclude that $10^{-5} \leq \beta \leq 10^1$. For our simulations, we chose the intermediate value of $\beta = 0.05$. Further, we must determine the value of the growth cone radius, R . Growth cone protrusions can extend between 5 μ m and 10.5 μ m from the axon shaft (Koch et al., 2012), where the shaft and the growth cone meet. For simplicity, we chose a growth cone radius of $R = L/2 \approx 16$ μ m, which corresponds to a relatively large growth cone.

We distinguish the two cases $\alpha_T > 1$ and $\alpha_T < 1$. When $\alpha_T > 1$ – see Fig. 7(a) – the durotactic force in the right region is greater than in the left region, thus the durotactic force component tends to pull the axon towards the right region. This results in a refractive behaviour with θ_2 smaller than θ_1 . Conversely, when $\alpha_T < 1$, both refraction and reflection can be observed, as shown in Fig. 7(b).

At a superficial level, these observations are reminiscent of the refractive and reflective behaviours of light rays crossing a sharp interface between two regions of different refractive indices. However, due to the finite size of the growth cone, the interaction with the interface is more complex and there is no simple quantitative analogy with Snell's law. Further, a fundamental difference between this model and geometric optics is that we do not have time-reversibility in our system. In optics, the time-reversal symmetry of Maxwell's equations implies that reflection occurs with $\theta_1 = \theta_2$. As can be seen in Figs. 7 and 8, this symmetry does not exist in our model, and in particular, we observe that $\theta_1 \neq \theta_2$ after reflection. In fact, when reflected, axons remain much more parallel to the interface than light rays do.

5.2. A simple stiffness gradient

Next we examine the case of an axon growing on a substrate with a graded stiffness of the form

$$\chi(x, y) = m_\chi y + \chi^*, \quad (53)$$

where the parameter m_χ is the stiffness gradient.

Firstly, as a simple illustration of growth on a graded substrate, we initiate multiple axons on the boundary of a disk in a linearly increasing stiffness field, mimicking the experimental setup in Koser et al. (2016). The growth pattern obtained matches qualitatively that seen experimentally; see Fig. 9, where axons are gradually deflected towards stiffer regions (upper parts of the domain).

More in general, the local traction exerted by the growth cone exhibits a maximum on the line D of optimal stiffness $y = 0$. We will show that D is a locally attracting set for our system in the sense that nearby trajectories are attracted asymptotically to D . This property is a consequence of the non-monotonic dependence of the traction force T upon the stiffness χ .

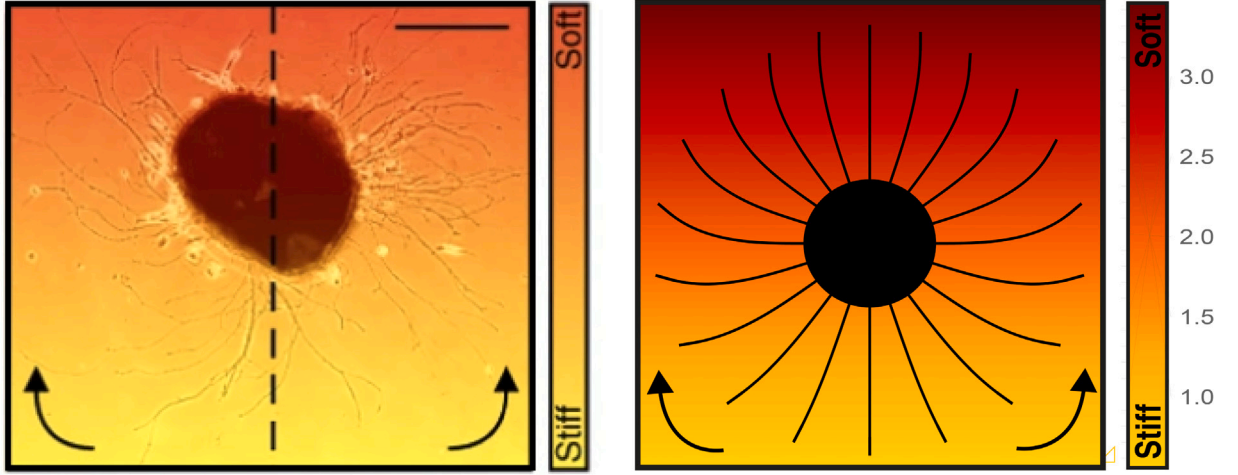


Fig. 9. (Left) Axons growing from a xenopus retina, cultured on a substrate with a linear stiffness gradient. As can be seen, the axons tend to grow more towards the soft side of the substrate (after Koser et al., 2016). (Right) Simulation of the rod model, with axons initialised on the boundary of a disc, in the stiffness field (53), showing qualitatively similar growth pattern. $m_\chi = -0.1$, $L = 32 \mu\text{m}$, $B = 10^{-19} \text{ N m}^2$, $R = L/2$, $\varphi_0 = \pi/2$, $\xi = f_0 K$, $M = 7.5 f_0 K$, $K = 1/(r^* e^{\gamma} \Gamma(0, r^*))$ and $2\rho R f_0 K H(r^*) = 10^{-9} \text{ N}$.

We consider an axon travelling in a neighbourhood of D with a typical width of order R , the radius of the growth cone. Hence, the growth cone is initially located at the position $\mathbf{r} = r R \mathbf{e}_y$, with r of order one, and travelling nearly parallel to the axis with $\mathbf{t} = \mathbf{e}_x + \psi \mathbf{e}_y + \dots$ with the growth cone angle $\psi \ll 1$. We obtain the behaviour of this axon by expanding the traction (30) about χ^* , while treating R and ψ as small parameters:

$$\begin{aligned} \rho^{-1} \mathbf{F}(\mathbf{r}, t) = & 2R \sin \varphi_0 T(\chi^*) \mathbf{t} + r^2 R^3 \sin \varphi_0 T''(\chi^*) m_\chi^2 \mathbf{t} + r R^3 \varphi_0 T''(\chi^*) m_\chi \mathbf{P}(\varphi_0) \nabla \chi \\ & + \frac{R^3 \varphi_0}{2} T''(\chi^*) \mathbb{P}(\varphi_0) : \nabla \chi \otimes \nabla \chi + O(R^4), \end{aligned} \quad (54)$$

where $\mathbb{P}(\varphi_0) := \int_{-\varphi_0}^{\varphi_0} \mathbf{e}_\varphi \otimes \mathbf{e}_\varphi \otimes \mathbf{e}_\varphi (d\varphi/\varphi_0)$, and $\mathbf{P}(\varphi_0)$ is defined in (32). Eq. (54) extends (31) to higher order. This is necessary for our analysis, since the leading-order deflection of $O(R^2)$ vanishes at $\chi = \chi^*$. Of particular interest is the transverse component $F_n := \mathbf{F} \cdot \mathbf{n}$, given by

$$F_n = \frac{1}{6} R^3 \rho T''(\chi^*) m_\chi^2 (3r(\varphi_0 - \sin \varphi_0 \cos \varphi_0) + 4\psi \sin^3 \varphi_0) + \text{h.o.t.} \quad (55)$$

Since $F_n = 0$ when $\psi = r = 0$, there exist trajectories along D (however, with a small drift appearing at higher orders and controlled by the third derivative $T'''(\chi^*)$). For $r \gg \psi$, the first term in the parentheses dominates, and, since $T''(\chi^*) < 0$, the deflection component has opposite sign of r and grows with r in magnitude. Thus we interpret this term as an elastic-like restoring force which pulls the axon back to the optimal stiffness line D . Conversely, very close to D , i.e. for $r \ll \psi$, the deflection is dominated by the second term and takes now the opposite sign of ψ , which, again, will tend to reorient the axon towards the horizontal. We conclude that, close to the line of optimal stiffness, durotaxis has a restoring, stabilising effect which tends to maintain the axon near this line.

Note, however, that the longitudinal component $F_t := \mathbf{F} \cdot \mathbf{t} \gg F_n$ dominates in the balance of forces, thus there may exist, in principle, conditions for which durotaxis will not suffice to keep the axon in the vicinity of D . Furthermore, it cannot be directly concluded whether the stable trajectory is attracting (exponential stability), or whether axons will oscillate around it and repeatedly overshoot it.

To further explore the dynamics of the axon near D , we perform numerical simulations shown in Fig. 10. Firstly, Fig. 10(a) illustrates that, in the vicinity of D and for small initial inclination, axons are attracted and converge towards this stable manifold. Second, Fig. 10(b) shows that there may exist an escape angle above which durotaxis is insufficient to keep the axon closer to D despite the negative durotaxis in that region. Clearly, if the axon crosses perpendicularly the line of optimal stiffness, it will not curve back. Whether nearby directions also escape in an infinite domain is neither easy to establish nor directly relevant to the problem. Indeed, in a much larger domain, it is possible that such trajectories curve back to the line of optimal stiffness. However, in a realistic scenario, such axons would have migrated away from the region of optimal stiffness and be subject to other stimuli.

In conclusion these examples illustrate that, even for a simple uniform gradient, the non-monotonic, nonlinear dependence of the locomotory force upon stiffness implies the existence of preferential regions where axons are expected to converge. Such a mechanism may be key to understanding neuronal focalisation towards regions of specific stiffness.

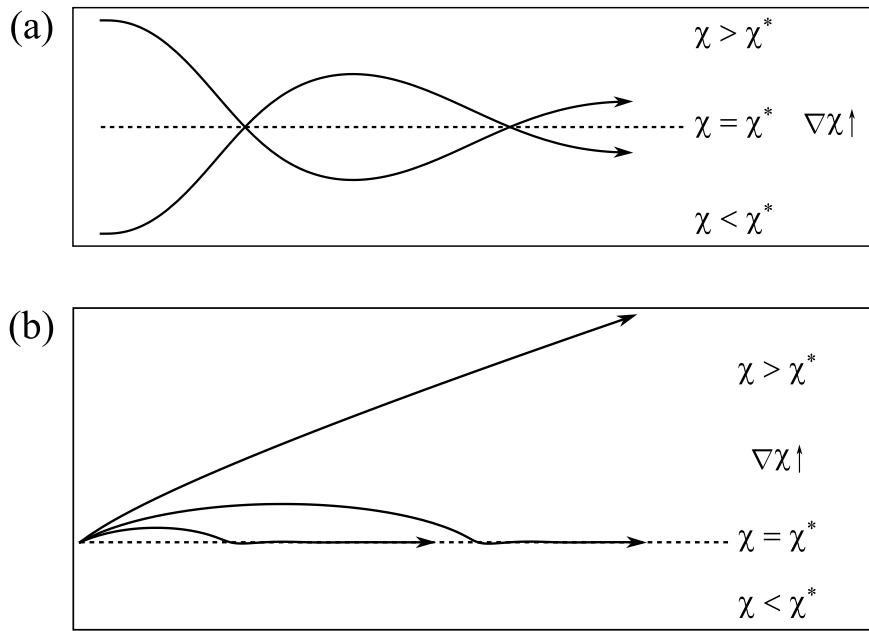


Fig. 10. (a) Axons trajectories converge to the line of optimal stiffness, D , if sufficiently close to it with sufficiently small inclination. (b) Axons with sufficiently large inclination escape the vicinity of D .

6. Biological applications

Taken together, these findings highlight two primary modes of guidance: deflective guidance (via reflection and refraction) and attractive guidance (via emergent attraction to regions of optimal stiffness). Lastly, we illustrate the potential role of these guidance modes in a biological scenario.

During early neurodevelopment, xenopus retinal ganglion cells (RGCs) establish connections with the brain as their axons exit the retina through the optic nerve and migrate towards the brain (Koser et al., 2016; Thompson et al., 2019). These axons grow collectively, cross the midline at the optic chiasm, and then travel along the contralateral brain surface towards the optic tectum, where they terminate. Towards the end of this journey, a postero-anterior gradient in brain tissue rigidity emerges, which strongly correlates with the stereotypical caudal turn observed in RGC axons as they traverse the mid-diencephalon en route to the tectum (Koser et al., 2016).

Oliveri et al. (2021) investigated the influence of this stiffness gradient on the deflection of an entire bundle of axons, under the assumption that the axons are mechanically coupled. In their model, differential stiffness sensing generates a velocity differential across the bundle's leading front, which explains its coordinated deflection. However, in biological systems, the mechanical coupling between axons is mediated by cell-cell adhesion, which is highly regulated and may be more or less loose (Šmít et al., 2017).

In this study, we address the problem from the opposite perspective by assuming the absence of mechanical coupling between axons in the bundle, which is compatible with a scenario where axons follow a leader cell (Hentschel and Van Ooyen, 1999). Using our model, we focus on the trajectories of individual axons, offering a complementary understanding of the role of stiffness gradients in axonal guidance.

To study the trajectory of single axons in the optic tract we use a brain rigidity field, $E(x, y)$ with unit of pressure, obtained by atomic force microscopy (Thompson et al., 2019; Oliveri et al., 2021). We investigate the trajectories of axons growing on a substrate with stiffness field $\chi(x, y) = E(x, y)/E_c$, where E_c is a characteristic stiffness. We simulated $N = 100$ axons, varying their initial position and direction around the entry point of the domain. The target zone (optic tectum) was defined as the quadrant seen in Fig. 11(c) and for each set of parameters we record the success rate N_s/N , characterising the ratio of axons successfully reaching the target (with number N_s) to the total number N .

In previous sections, we showed that the key features of the traction-stiffness curve $T(\chi)$ relating to axon guidance are χ^* , $T''(\chi^*)$, and T_∞ . These features can be directly controlled through myosin contractility M (see Section 2.3) which can be targetted through pharmacological treatments in experiments such as application of the myosin inhibitor blebbistatin (Kovács et al., 2004), or by modulating the number of myosin molecules; or via the clutch properties (Bangasser et al., 2013, 2017).

Here we investigated the effect of myosin contractility on the success rate and found that success rate is a non-monotonic function of M . The analysis of the success rate as a function of contractility allows us to identify four regimes depending on M , where the success rate is in turn decreasing, constant, increasing and decreasing again; see Fig. 11(a).

We can understand this non-monotonic behaviour by looking at the resulting traction field $T(E(x, y)/E_c)$ in the four different regimes. We investigate a representative case from each regime; (i)–(iv) in Fig. 11(a). In the domain, the rigidity ranges from 57 Pa to

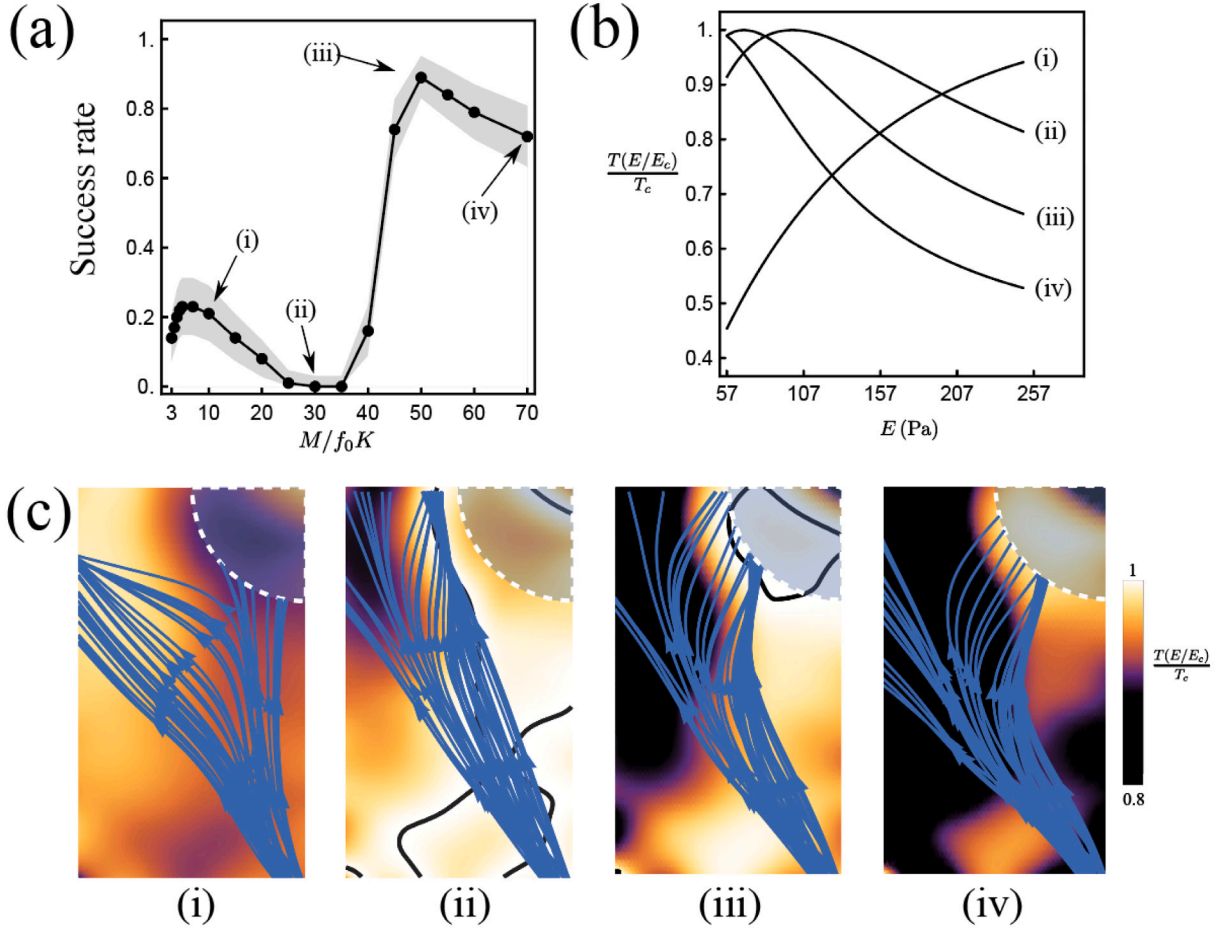


Fig. 11. (a) Success rate as a function of M . (b) Traction as a function of E for the values of M indicated in (a). (c) Density map of traction for the values of M indicated in (a) overlaid with representative trajectories of axons for the given parameters. $L = 32 \mu\text{m}$, $B = 10^{-19} \text{ N m}^2$, $R = L/2$, $\varphi_0 = \pi/2$, $\xi = f_0K$, $K = 1/2$, $2\rho R f_0KH(r)^* = 10^{-9} \text{ N}$, $T_c = f_0KH(r)^*$ and $E_c = 6 \text{ kPa}$.

250 Pa. For $M/f_0K = 10$, the optimal stiffness is greater than 250 Pa. Therefore, traction is an increasing function of rigidity between 57 Pa and 250 Pa; see (i) in Fig. 11(b). Since the left side of the domain is stiffer than the right side, the traction $T(E(x, y)/E_c)$ smoothly increases from right to left. As a result, axons undergo positive durotaxis and are attracted to the left side of the domain leading to a poor success rate of 21%.

As M/f_0K increases further, the optimal stiffness decreases and enters the range of stiffness values present in the domain; see (ii) and (iii) in Fig. 11(b). As a result, contours of optimal stiffness form within the domain and axons tend to follow them. In the case of $M/f_0K = 35$, one of these contours leads most of the axons away from the target leading to a catastrophic success rate of 0%; see Fig. 11(c), (ii).

For greater values of M/f_0K , with the optimal stiffness decreasing further and the decay of $T(E/E_c)$ to T_∞ becoming faster, the domain becomes roughly bisected by an interface with a region of high traction on the right side of the domain and a region of low traction on the left side of the domain. This situation is similar to the example studied in Section 5.1 where axons can reflect against a sharp interface between regions of different rigidities. Indeed, we see that for $M/f_0K = 50$, most axons reflect against a well-formed interface between the two regions of low and high traction, and reach the target; see Fig. 11(c), (iii). Because the interface is not perfectly straight, many axons that are not initially reflected by their interaction with the interface, re-approach the interface later on. In this case, the axons are refracted into the region of high traction and subsequently reach the target. This combination of reflection and refraction results in the high success rate of 89%. For $M/f_0K > 50$, a combination of reflection and refraction again results in high success rate. However, the placement of the interface is less favourable and fewer axons reach the target; see Fig. 11(c), (iv).

These simulations suggest that durotaxis may play a role in guiding the optic tract to the tectum. However, obtaining accurate parameter estimates remains a significant challenge, making it difficult to draw definitive conclusions about the precise role of durotaxis in this process. Additionally, collective effects and chemotaxis are well-established as dominant mechanisms in optic tract guidance.

Nonetheless, the results illustrate how paradigms such as reflection, refraction, and the tracking of lines of optimal stiffness can, in principle, guide axons in biologically realistic scenarios. Furthermore, the findings underscore the critical role of the traction stiffness curve $T(\chi)$ in controlling the dynamics. As emphasised in this paper, axonal trajectories in durotaxis are dictated by the stiffness field and the three key properties of the traction stiffness curve: χ^* , $T''(\chi^*)$, and T_∞ . The choice of these properties (e.g. via the parameter M) control the outcomes. Our results suggest that, under the proposed model of durotaxis, the most plausible mechanism for guiding axons to the optic tract involves a combination of reflection and refraction, rather than following lines of optimal stiffness.

7. Discussion

Axons are examples of active structures that process multiple and complex stimuli and dynamically adapt their growth to these stimuli, a process similar to tropic phenomena in plants (Moulton et al., 2020) or the response of soft liquid crystal elastomer rods (Goriely et al., 2023). The problem is then to model the evolution, growth, deformation, and motion of such a structure.

Here we adopted a multiscale approach to model the migration of an axon, combining (i) the molecular interaction between an axon and its substrate; (ii) the integration of such interactions over the growth cone to obtain the forces acting at the tip of the axon; (iii) modelling the growing axon as a morphoelastic rod in response to both stimuli and interaction with its environment; and (iv) simplifying this model for computational purposes based on the fact that growth takes place close the growth cone.

In contrast with many models for axon guidance based on Brownian-type dynamics (see Maskery and Shinbrot, 2005; Oliveri and Goriely, 2022, and references therein), growth is modelled explicitly, as well as the mechanics of axonal shaft bending and elongation, and the mechanics of cell adhesion underlying locomotion. The primary challenge in constructing a mechanistic model of axonal guidance lies in simultaneously accounting for axonal mechanics, growth cone mechanics, and actomyosin dynamics. To address this problem, we adopt a multiscale, mean-field framework. Following Chan and Odde (2008) and Sens (2013), we begin by modelling the fundamental interaction between a single actin filament and the substrate. This local interaction law is then employed in a second step to derive the total force exerted across the growth cone.

Crucially, we do not model explicitly the entire actin–myosin lamellipodium by taking into account each individual actin filament, but, instead, we derive a minimal expression for the growth cone traction in a shallow stiffness gradient. This approach contrasts with models such as Aeschlimann (2000), where individual filaments are represented explicitly in a computational framework. By integrating this growth cone force with a reduced beam model, which accounts for the gradual fixation of the axon to its substrate and incorporates a finite distal growth zone, we obtain a simple tractable model that can be easily implemented.

This approach reveals key guiding principles of durotaxis. First, the mechanical interaction between the axon and the substrate, governed by Bell-type adhesion kinetics, produces a highly nonlinear and potentially non-monotonic dependence of the force T generated by an actin filament on substrate stiffness. Such previously-identified non-monotonicity (Chan and Odde, 2008; Sens, 2013; Bangasser and Odde, 2013) arises from a phenomenon known as *stick-slip instability*, where excessive stiffness leads to rapid breakage of cross-linkers, reducing the generated force compared to more moderate stiffness levels. Critically, this non-monotonic behaviour of T is essential for explaining the coexistence of positive and negative durotactic regimes, which can arise without the need for separate cellular mechanisms.

At the cellular scale, this behaviour implies the existence of stable, attractive regions with optimal stiffness where axons are likely to converge due to enhanced adhesion. Notably, the idea that a simple stiffness gradient can create distinct regions via nonlinear cellular sensing strongly parallels patterning mechanisms such as Wolpert's *French flag* model (Wolpert, 2008). This analogy may hold particular significance for understanding mechanically induced neuronal segmentation, as observed by Schaeffer et al. (2022).

Second, inspired by the analogy proposed by Oliveri et al. (2021), we demonstrate that axons encountering a straight stiffness interface may exhibit behaviours analogous to optical refraction or reflection, depending on the incidence angle and mechanical conditions. This observation raises the intriguing possibility of interpreting durotactic guidance through mechanisms analogous to optical lensing or channelling, albeit governed by laws distinct from Snell's law. This opens an exciting avenue for future research to uncover the broader principles of “axonal optics” that emerge from this model.

Axonal growth is a highly complex cellular process, influenced by numerous interdependent signals and growth conditions, and is inherently noisy. In such a context, the prospect of establishing simple, universal laws that capture the detailed intricacies of axonal guidance may appear unattainable. Nevertheless, by employing a minimal set of assumptions grounded in first principles and biological observations, we uncovered fundamental qualitative principles that govern durotaxis.

Our multiscale framework is a general theory that integrates microscale interactions between axons and substrate with macroscale motion. It is presented here in the simplest setting and, as such, is not designed to replicate particular experiments in details. Yet, achieving more quantitative applications is possible but will require extending the model to account for additional factors, such as chemotactic influences—particularly the poorly understood interplay between chemotactic sensitivity and mechanics (Franze, 2020); steric interactions with other cells; the mechanical characteristics and particularities of different substrates in both two and three dimensions (Santos et al., 2020); more intricate axonal behaviours, such as contraction and collapse (Recho et al., 2016); stochastic effects; domain curvature and its influence on cell growth (Smeal et al., 2005); and collective chemical and mechanical phenomena (De Gennes, 2007; Hentschel and Van Ooyen, 1999; Chaudhuri et al., 2011).

Despite these phenomenological limitations, the proposed model provides a foundational framework and a key step towards a comprehensive, multiscale and multiphysics field theory of axonal development that can be scaled up to the entire brain.

CRediT authorship contribution statement

Christoforos Kassianides: Writing – review & editing, Writing – original draft, Visualization, Validation, Software, Methodology, Investigation, Funding acquisition, Formal analysis, Conceptualization. **Alain Goriely:** Writing – review & editing, Writing – original draft, Visualization, Supervision, Project administration, Methodology, Funding acquisition, Formal analysis, Conceptualization. **Hadrien Oliveri:** Writing – review & editing, Writing – original draft, Visualization, Validation, Supervision, Software, Project administration, Methodology, Investigation, Formal analysis, Conceptualization.

Declaration of competing interest

The authors declare that they have no known competing financial interests or personal relationships that could have appeared to influence the work reported in this paper.

Acknowledgements

C.K. acknowledges funding through a studentship from the Engineering and Physical Sciences Research Council (EPSRC), United Kingdom under project reference 2580825. The authors thank Kristian Franze for insightful discussions.

Appendix A. Derivation of the beam model

Here we derive the evolution laws for the dynamic section modelled by an inextensible growing beam (Section 4.2). The dynamic distal section of the axon is represented by a spatial curve $\mathbf{r}(\sigma, t)$ given as

$$\mathbf{r}(\sigma, t) = \hat{\mathbf{r}}(t) + x(\sigma, t) \hat{\mathbf{t}}(t) + y(\sigma, t) \hat{\mathbf{v}}(t) \quad (56)$$

Here, $\sigma \in [0, L]$ measures the arclength from the base of the dynamic section; and where $\hat{\mathbf{r}}$, $\hat{\mathbf{t}}$ and $\hat{\mathbf{v}}$ indicate respectively the position, and the tangent and normal vectors to the curve at $\sigma = 0$. The coordinates x and y indicate the position of the curve in the local frame $\{\hat{\mathbf{t}}, \hat{\mathbf{v}}\}$. These definitions imply the boundary conditions

$$x(0, t) = y(0, t) = 0, \quad \frac{\partial x}{\partial \sigma}(0, t) = 1, \quad \frac{\partial y}{\partial \sigma}(0, t) = 0. \quad (57)$$

Further, x, y can be obtained by integrating the system

$$\frac{\partial x}{\partial \sigma} = \cos \theta, \quad \frac{\partial y}{\partial \sigma} = \sin \theta, \quad (58)$$

where $\theta(\sigma, t)$ indicates the polar angle of the tangent $\partial \mathbf{r} / \partial \sigma$ at arclength σ and time t , in the local frame $\{\hat{\mathbf{t}}, \hat{\mathbf{v}}\}$. That is,

$$\frac{\partial \mathbf{r}}{\partial \sigma} = \cos \theta \hat{\mathbf{t}} + \sin \theta \hat{\mathbf{v}}. \quad (59)$$

During a small time increment ΔT we update the shape of the axon by first evolving the curve according to the over-damped beam equations (61), assuming that the axon is clamped at $\hat{\mathbf{r}}(t)$ with angle $\hat{\theta}(t)$, and subject to the force $\mathbf{F}(t)$ applied at $\sigma = L$ with zero torque. We introduce the auxiliary function

$$\tilde{\mathbf{r}}(\sigma, T, t) = \hat{\mathbf{r}}(t) + \tilde{x}(\sigma, T, t) \hat{\mathbf{t}} + \tilde{y}(\sigma, T, t) \hat{\mathbf{v}}. \quad (60)$$

Here, $\tilde{\mathbf{r}}(\sigma, T, t)$ describes the evolution of the axon profile, in time T , with initial condition $\mathbf{r}(\sigma, t)$ and clamp angle $\hat{\theta}(t)$, subjected to constant force $\mathbf{F}(t)$. The functions $\tilde{x}(\sigma, T, t)$ and $\tilde{y}(\sigma, T, t)$ satisfy the over-damped beam equations in the frame $\{\hat{\mathbf{t}}, \hat{\mathbf{v}}\}$, with spatial variable σ and time variable T .

$$B \frac{\partial^2 \tilde{\theta}}{\partial \sigma^2} + \tilde{n}_y \cos \tilde{\theta} - \tilde{n}_x \sin \tilde{\theta} = 0, \quad (61a)$$

$$\frac{\partial \tilde{n}_x}{\partial \sigma} = \zeta \frac{\partial \tilde{x}}{\partial T}, \quad \frac{\partial \tilde{n}_y}{\partial \sigma} = \zeta \frac{\partial \tilde{y}}{\partial T}, \quad (61b)$$

$$\frac{\partial \tilde{x}}{\partial \sigma} = \cos \tilde{\theta}, \quad \frac{\partial \tilde{y}}{\partial \sigma} = \sin \tilde{\theta}, \quad (61c)$$

where \tilde{n}_x and \tilde{n}_y are the components of the internal resultant force $\tilde{\mathbf{n}} = \tilde{n}_x \hat{\mathbf{t}} + \tilde{n}_y \hat{\mathbf{v}}$ at time T . We enforce the boundary and initial conditions

$$\tilde{n}_x(L, T, t) = \mathbf{F}(t) \cdot \hat{\mathbf{t}}(t), \quad \tilde{n}_y(L, T, t) = \mathbf{F}(t) \cdot \hat{\mathbf{v}}(t), \quad (62a)$$

$$\tilde{\theta}(0, T, t) = 0, \quad \frac{\partial \tilde{\theta}}{\partial \sigma}(L, T, t) = 0, \quad (62b)$$

$$\tilde{x}(0, T, t) = 0, \quad \tilde{y}(0, T, t) = 0, \quad (62c)$$

$$\bar{x}(\sigma, 0, t) = x(\sigma, t), \quad \bar{y}(\sigma, 0, t) = y(\sigma, t). \quad (62d)$$

From here, we can update the axon's shape according to (61) integrated over a small time increment ΔT . That is, we define an intermediate curve

$$\bar{\mathbf{r}}_{\text{inter}}(\sigma) = \bar{\mathbf{r}}(\sigma, \Delta T, t). \quad (63)$$

The updated axon after growth is then obtained by advancing the clamp position along this intermediate profile by a small length $\Delta\sigma = c(t)\Delta T$,

$$\mathbf{r}(\sigma, t + \Delta T) = \bar{\mathbf{r}}_{\text{inter}}(\sigma + \Delta\sigma). \quad (64)$$

Expanding the r.h.s. to second order in ΔT , rearranging the terms and taking the limit $\Delta T \rightarrow 0$, we obtain

$$\begin{aligned} \frac{\partial \mathbf{r}}{\partial t}(\sigma, t) = & \left(c(t) \frac{\partial \bar{x}}{\partial \sigma}(\sigma, 0, t) + \frac{\partial \bar{x}}{\partial T}(\sigma, 0, t) \right) \hat{\mathbf{r}} \\ & + \left(c(t) \frac{\partial \bar{y}}{\partial \sigma}(\sigma, 0, t) + \frac{\partial \bar{y}}{\partial T}(\sigma, 0, t) \right) \hat{\mathbf{v}}. \end{aligned} \quad (65)$$

Differentiating (56) we derive

$$\frac{\partial \mathbf{r}}{\partial t}(\sigma, t) = \frac{d\hat{\mathbf{r}}}{dt} + \left(\frac{\partial x}{\partial t} - y \frac{d\hat{\theta}}{dt} \right) \hat{\mathbf{r}} + \left(\frac{\partial y}{\partial t} + x \frac{d\hat{\theta}}{dt} \right) \hat{\mathbf{v}}, \quad (66)$$

where $\hat{\theta}$ is the angle between $\hat{\mathbf{r}}$ and the horizontal direction. Equating the r.h.s. of (65) and (66) we obtain

$$\frac{\partial x}{\partial t} - y \frac{d\hat{\theta}}{dt} + \frac{\partial \hat{\mathbf{r}}}{\partial t} \cdot \hat{\mathbf{r}} = c(t) \frac{\partial \bar{x}}{\partial \sigma}(\sigma, 0, t) + \frac{\partial \bar{x}}{\partial T}(\sigma, 0, t), \quad (67a)$$

$$\frac{\partial y}{\partial t} + x \frac{d\hat{\theta}}{dt} + \frac{\partial \hat{\mathbf{r}}}{\partial t} \cdot \hat{\mathbf{v}} = c(t) \frac{\partial \bar{y}}{\partial \sigma}(\sigma, 0, t) + \frac{\partial \bar{y}}{\partial T}(\sigma, 0, t). \quad (67b)$$

To obtain the evolution equation for $\hat{\mathbf{r}}$ we set $\sigma = 0$ in the above equations. We note that, due to (57), we have $\partial x / \partial t(0, t) = \partial y / \partial t(0, t) = 0$ and so

$$\frac{\partial \hat{\mathbf{r}}}{\partial t} = c(t) \hat{\mathbf{r}} \quad (68)$$

We derive the evolution equation for $\hat{\theta}$ by imposing (to first order in ΔT) that

$$\frac{\partial \mathbf{r}}{\partial \sigma}(0, t + \Delta T) = \frac{\partial \mathbf{r}}{\partial \sigma}(c(t)\Delta T, t). \quad (69)$$

Expanding the l.h.s. in t and the r.h.s. in σ to second order in ΔT , rearranging and taking the limit $\Delta T \rightarrow 0$ gives

$$\frac{d}{dt} \left(\frac{\partial \mathbf{r}}{\partial \sigma}(0, t) \right) = c(t) \frac{\partial^2 \mathbf{r}}{\partial \sigma^2}(0, t), \quad (70)$$

which simplifies to

$$\frac{\partial^2 x}{\partial \sigma^2}(0, t) = 0, \quad (71a)$$

$$\frac{d\hat{\theta}}{dt} = c(t) \frac{\partial^2 y}{\partial \sigma^2}(0, t). \quad (71b)$$

Therefore the governing equations become

$$\frac{\partial x}{\partial t} - yc(t) \frac{\partial^2 y}{\partial \sigma^2}(0, t) + c(t) = c(t) \frac{\partial \bar{x}}{\partial \sigma}(\sigma, 0, t) + \frac{\partial \bar{x}}{\partial T}(\sigma, 0, t), \quad (72a)$$

$$\frac{\partial y}{\partial t} + xc(t) \frac{\partial^2 y}{\partial \sigma^2}(0, t) = c(t) \frac{\partial \bar{y}}{\partial \sigma}(\sigma, 0, t) + \frac{\partial \bar{y}}{\partial T}(\sigma, 0, t). \quad (72b)$$

Next, we assume that the normal component of the force \mathbf{F} w.r.t. the clamp axis is small. That is,

$$\mathbf{F} \cdot \hat{\mathbf{v}} = \epsilon N_y, \quad (73)$$

for $\epsilon \ll 1$ and where $\mathbf{F} \cdot \hat{\mathbf{r}}$ and N_y are $O(1)$. Consequently, the axon is subject to small deflections from the axis spanned by $\hat{\mathbf{r}}$. i.e.

$$x = \sigma + O(\epsilon^2), \quad y = \epsilon Y(\sigma, t) + O(\epsilon^2), \quad \theta = \epsilon \Theta(\sigma, t) + O(\epsilon^2), \quad (74)$$

for $\epsilon \ll 1$. Plugging (74) into (72) we obtain

$$\frac{\partial \bar{x}}{\partial T}(\sigma, 0, t) = O(\epsilon^2), \quad (75a)$$

$$\frac{\partial \bar{y}}{\partial T}(\sigma, 0, t) - \epsilon \left(\dot{Y} + \sigma c(t) \frac{\partial^2 Y}{\partial \sigma^2}(0, t) - c(t) \frac{\partial Y}{\partial \sigma} \right) = O(\epsilon^2). \quad (75b)$$

For the next step, it is important to note that since we have $\partial y / \partial \sigma = \sin \theta$ and $\tilde{y}(\sigma, 0, t) = y(\sigma, t)$, it follows that $\partial \tilde{y} / \partial \sigma(\sigma, 0, t) = \partial y / \partial \sigma$ and therefore

$$\tilde{\theta}(\sigma, 0, t) = \theta(\sigma, t). \quad (76)$$

We can now obtain an expression for $\partial \tilde{y} / \partial T(\sigma, 0, t)$ to first order in ϵ . Positing

$$\tilde{\theta}(\sigma, 0, t) = \theta(\sigma, t) = \epsilon \Theta(\sigma, t) + O(\epsilon^2). \quad (77)$$

with Θ a function of order unit, using (61a) and (61c), and differentiating w.r.t. σ , we obtain

$$\epsilon B \frac{\partial^3 \Theta}{\partial \sigma^3} + \frac{\partial \tilde{n}_y}{\partial \sigma} - \tilde{n}_x \frac{\partial^2 \tilde{y}}{\partial \sigma^2}(\sigma, 0; t) = O(\epsilon^2), \quad (78)$$

which is equivalent to the beam equation

$$\epsilon B \frac{\partial^4 Y}{\partial \sigma^4} + \zeta \frac{\partial \tilde{y}}{\partial T} - \epsilon \tilde{n}_x \frac{\partial^2 Y}{\partial \sigma^2} = O(\epsilon^2). \quad (79)$$

Thus,

$$\frac{\partial \tilde{y}}{\partial T}(\sigma, 0; t) = \frac{\epsilon}{\zeta} \left(\tilde{n}_x \frac{\partial^2 Y}{\partial \sigma^2} - B \frac{\partial^4 Y}{\partial \sigma^4} \right) + O(\epsilon^2). \quad (80)$$

To leading order we thus have

$$\frac{\partial Y}{\partial t} - c(t) \frac{\partial Y}{\partial \sigma} = \frac{1}{\zeta} \left(F(t) \cdot \hat{\tau} \frac{\partial^2 Y}{\partial \sigma^2} - B \frac{\partial^4 Y}{\partial \sigma^4} \right) - \sigma c(t) \frac{\partial^2 Y}{\partial \sigma^2}(0, t). \quad (81)$$

We obtain the first three boundary conditions for Y by evaluating (62b) and (62c) at $T = 0$, to first order in ϵ , giving

$$Y(0, t) = 0, \quad \frac{\partial Y}{\partial \sigma}(0, t) = 0, \quad \frac{\partial^2 Y}{\partial \sigma^2}(L, t) = 0. \quad (82)$$

The fourth boundary condition for Y is obtained similarly, by evaluating (61a) at $\sigma = L$ and $T = 0$, to $O(\epsilon)$,

$$B \frac{\partial^3 Y}{\partial \sigma^3}(L, t) - F \cdot \hat{\tau} \frac{\partial Y}{\partial \sigma}(L, t) = -N_y. \quad (83)$$

Eq. (81) along with boundary conditions (82), (83) constitute the linearised system for Y under small deflections. Multiplying each of these equations by ϵ , we obtain the linearised equation for y , to first order in ϵ . The full system is then

$$\frac{\partial \hat{\tau}}{\partial t} = c(t) \hat{\tau}, \quad (84a)$$

$$\frac{\partial \hat{\theta}}{\partial t} = c(t) \frac{\partial^2 y}{\partial \sigma^2}(0, t), \quad (84b)$$

$$\frac{\partial y}{\partial t} - c(t) \frac{\partial y}{\partial \sigma} = \frac{1}{\zeta} \left(F(t) \cdot \hat{\tau} \frac{\partial^2 y}{\partial \sigma^2} - B \frac{\partial^4 y}{\partial \sigma^4} \right) - \sigma c(t) \frac{\partial^2 y}{\partial \sigma^2}(0, t), \quad (84c)$$

$$y(0, t) = 0, \quad \frac{\partial y}{\partial \sigma}(0, t) = 0, \quad \frac{\partial^2 y}{\partial \sigma^2}(L, t) = 0, \quad (84d)$$

$$B \frac{\partial^3 y}{\partial \sigma^3}(L, t) - F \cdot \hat{\tau} \frac{\partial y}{\partial \sigma}(L, t) = -F \cdot \hat{v}. \quad (84e)$$

These equations make up the system (47) used in the main text.

Appendix B. Numerics and implementation details

To solve the system for $(\hat{r}, \hat{\theta}, y)$ we spatially discretise (47a) using a spectral method. This approach approximates the derivatives of a given function by the derivatives of a Chebyshev polynomial interpolation of that function on a discrete grid (Trefethen, 2000; Press et al., 2007). To that end, we first transform the spatial domain to the interval $[-1, 1]$. We start by rewriting (47a) in terms of the dimensionless variable

$$X = 2\sigma/L - 1 \in [-1, 1]. \quad (85)$$

This allows us to discretise the spatial domain according to the Chebyshev grid (Trefethen, 2000)

$$X_j = \cos(j\pi/N), \quad j = 0, \dots, N. \quad (86)$$

Thus, we can convert the PDE (47a) into a system of ordinary differential equations. First, we define

$$y_j(t) = y(X_j, t), \quad (87)$$

and the vector

$$\mathbf{y} = (y_0, \dots, y_N). \quad (88)$$

The spatial derivatives of $y(X, t)$ evaluated on the Chebyshev grid may be approximated by multiplying \mathbf{y} with the Chebyshev differentiation matrix D_N (Trefethen, 2000). e.g.

$$\frac{\partial^k y}{\partial X^k}(X_j, t) \approx [D_N^k \mathbf{y}]_j. \quad (89)$$

By replacing instances of the spatial derivatives of $y(X, t)$ with the above approximation in the rescaled equation, we obtain an ordinary differential equation for $\mathbf{y}(t)$ of the form

$$\frac{d\mathbf{y}}{dt} = \mathbf{g}(t, \hat{\theta}, \hat{\mathbf{r}}, \mathbf{y}). \quad (90)$$

Once instances of spatial derivatives have been replaced according to (89), the boundary conditions constitute conditions that \mathbf{y} must satisfy. Solving these equations for y_0, y_1, y_{N-1}, y_N in terms of y_2, \dots, y_{N-2} ensures that \mathbf{y} satisfies these conditions.

Using the boundary conditions we can constrain y_0, y_1, y_{N-1} and y_N . The first three boundary conditions,

$$y(0, t) = 0, \quad \frac{\partial y}{\partial \sigma}(0, t) = 0, \quad \frac{\partial^2 y}{\partial \sigma^2}(L, t) = 0. \quad (91)$$

are linear, which allows to express directly y_1, y_{N-1}, y_N in terms of y_0, y_2 , and y_{N-2} .

$$B \frac{\partial^3 y}{\partial \sigma^3}(L, t) - \mathbf{F} \cdot \hat{\mathbf{r}} \frac{\partial y}{\partial \sigma}(L, t) = -\mathbf{F} \cdot \hat{\mathbf{v}}, \quad (92)$$

can be discretised as

$$B(2/L)^3 [D_N^3 \mathbf{y}]_0 - (2/L) \mathbf{F} \cdot \hat{\mathbf{r}} [D_N \mathbf{y}]_0 = -\mathbf{F} \cdot \hat{\mathbf{v}}, \quad (93)$$

noting that $\partial^k y / \partial X^k = (L/2)^k \partial^k y / \partial \sigma^k$ (85). Here, \mathbf{F} depends on the position of the tip, thus (93) is a nonlinear equation for y_0 for which no closed-form solution can be found in general. In principle, one can solve this nonlinear equation numerically for y_0 using a root-finding procedure at each time step. Alternatively, we may simplify the problem by evaluating the tangent at the tip at the neighbouring point $X = X_2$ (instead of X_1), i.e.,

$$\mathbf{t} = \frac{\partial \mathbf{r} / \partial \sigma(L, t)}{\|\partial \mathbf{r} / \partial \sigma(L, t)\|} \approx \left(1 + \left(\frac{2}{L} \frac{y_2 - y_3}{X_2 - X_3} \right)^2 \right)^{-1/2} \left(\hat{\mathbf{r}} + \frac{2}{L} \frac{y_2 - y_3}{X_2 - X_3} \hat{\mathbf{v}} \right), \quad (94)$$

so as to eliminate the explicit dependence upon y_0 . The error produced by the approximation (94) for the tangent is $O(1/N^2)$ as $N \rightarrow \infty$. This converts the above equation to a linear one, which allows us to obtain a closed-form expression for y_0 in terms of y_2, \dots, y_{N-2} .

Thus, (47a) can be approximated by an equation of the form

$$\frac{d\mathbf{Y}}{dt} = \mathbf{G}(t, \hat{\theta}, \hat{\mathbf{r}}, \mathbf{Y}), \quad (95)$$

where $\mathbf{Y} := (y_2, \dots, y_{N-2})$ denotes the vector of discrete variables after truncation of the boundary values y_0, y_1, y_N and y_{N-1} (which are now fixed); and $\mathbf{G}(t, \hat{\theta}, \hat{\mathbf{r}}, \mathbf{Y}) := \mathbf{g}(t, \hat{\theta}, \hat{\mathbf{r}}, \mathbf{y}(\mathbf{Y}))$. Finally, (47b) can be re-written as

$$\frac{d\hat{\theta}}{dt} = (2/L)^2 c(t) [D_N^2 \mathbf{y}]_N, \quad (96)$$

and (47c) remains unchanged. The equations

$$\frac{d\mathbf{Y}}{dt} = \mathbf{G}(t, \hat{\theta}, \hat{\mathbf{r}}, \mathbf{Y}), \quad (97a)$$

$$\frac{d\hat{\theta}}{dt} = (2/L)^2 c(t) [D_N^2 \mathbf{y}]_N, \quad (97b)$$

$$\frac{d\hat{\mathbf{r}}}{dt} = c(t) \hat{\mathbf{r}}, \quad (97c)$$

form a simple IVP which which can be integrated numerically (here we used the built-in function *NDSolve* implemented in *Mathematica* 13.3).

Data availability

No data was used for the research described in the article.

References

- Aeschlimann, M., 2000. Biophysical Model of Axonal Pathfinding (Ph.D. thesis). University of Lausanne, Department of Theoretical Physics.
- Bangasser, B.L., Odde, D.J., 2013. Master equation-based analysis of a motor-clutch model for cell traction force. *Cell. Mol. Bioeng.* 6, 449–459. <http://dx.doi.org/10.1007/s12195-013-0296-5>.

- Bangasser, B.L., Rosenfeld, S.S., Odde, D.J., 2013. Determinants of maximal force transmission in a motor-clutch model of cell traction in a compliant microenvironment. *Biophys. J.* 105, 581–592. <http://dx.doi.org/10.1016/j.bpj.2013.06.027>, URL: [https://www.cell.com/biophysj/fulltext/S0006-3495\(11\)00376-6](https://www.cell.com/biophysj/fulltext/S0006-3495(11)00376-6).
- Bangasser, B.L., Shamsan, G.A., Chan, C.E., Opoku, K.N., Tüzel, E., Schlichtmann, B.W., Kasim, J.A., Fuller, B.J., McCullough, B.R., Rosenfeld, S.S., et al., 2017. Shifting the optimal stiffness for cell migration. *Nat. Commun.* 8 (15313), <http://dx.doi.org/10.1038/ncomms15313>, URL: <https://www.nature.com/articles/ncomms15313>.
- Bell, G.I., 1978. Models for the specific adhesion of cells to cells. *Science* 200, 618–627. <http://dx.doi.org/10.1126/SCIENCE.347575>, URL: <https://www.science.org/doi/10.1126/science.347575>.
- Bell, G.I., Dembo, M., Bongrand, P., 1984. Cell adhesion. competition between nonspecific repulsion and specific bonding. *Biophys. J.* 45, 1051–1064. [http://dx.doi.org/10.1016/S0006-3495\(84\)84252-6](http://dx.doi.org/10.1016/S0006-3495(84)84252-6), URL: [https://www.cell.com/biophysj/pdf/S0006-3495\(84\)84252-6](https://www.cell.com/biophysj/pdf/S0006-3495(84)84252-6).
- Bressloff, P.C., 2020. Stochastic resetting and the mean-field dynamics of focal adhesions. *Phys. Rev. E* 102, 022134. <http://dx.doi.org/10.1103/PhysRevE.102.022134>, URL: <https://journals.aps.org/pre/abstract/10.1103/PhysRevE.102.022134>.
- Chan, C.E., Odde, D.J., 2008. Traction dynamics of filopodia on compliant substrates. *Science* 322, 1687–1691. <http://dx.doi.org/10.1126/science.1163595>, URL: <https://www.science.org/doi/10.1126/science.1163595>.
- Chaudhuri, D., Borowski, P., Zapotocky, M., 2011. Model of fasciculation and sorting in mixed populations of axons. *Phys. Rev. E—Stat. Nonlinear, Soft Matter Phys.* 84, 021908. <http://dx.doi.org/10.1103/PhysRevE.84.021908>, URL: <https://journals.aps.org/pre/abstract/10.1103/PhysRevE.84.021908>.
- De Gennes, P.G., 2007. Collective neuronal growth and self organization of axons. *Proc. Natl. Acad. Sci. USA* 104, 4904–4906. <http://dx.doi.org/10.1073/pnas.0609871104>, URL: <https://www.pnas.org/doi/full/10.1073/pnas.0609871104>.
- Dennerll, T.J., Lamoureux, P., Buxbaum, R.E., Heidemann, S.R., 1989. The cytomechanics of axonal elongation and retraction. *J. Cell. Biol.* 109, 3073–3083. <http://dx.doi.org/10.1083/jcb.109.6.3073>, URL: <https://rupress.org/jcb/article-abstract/109/6/3073/28999>.
- Elosegui-Artola, A., Trepas, X., Roca-Cusachs, P., 2018. Control of mechanotransduction by molecular clutch dynamics. *Trends Cell Biol.* 28, 356–367. <http://dx.doi.org/10.1016/j.tcb.2018.01.008>, URL: [https://www.cell.com/trends/cell-biology/fulltext/S0962-8924\(18\)30017-5](https://www.cell.com/trends/cell-biology/fulltext/S0962-8924(18)30017-5).
- Espina, J.A., Marchant, C.L., Barriga, E.H., 2022. Durotaxis: the mechanical control of directed cell migration. *FEBS J.* 289, 2736–2754. <http://dx.doi.org/10.1111/febs.15862>, URL: <https://febs.onlinelibrary.wiley.com/doi/10.1111/febs.15862>.
- Franze, K., 2020. Integrating chemistry and mechanics: The forces driving axon growth. *Annu. Rev. Cell. Dev. Biol.* 36, 61–83. <http://dx.doi.org/10.1146/annurev-cellbio-100818-125157>, URL: <https://www.annualreviews.org/content/journals/10.1146/annurev-cellbio-100818-125157>.
- Franze, K., Guck, J., 2010. The biophysics of neuronal growth. *Rep. Progr. Phys.* 73, <http://dx.doi.org/10.1088/0034-4885/73/9/094601>.
- Goriely, A., 2017. The Mathematics and Mechanics of Biological Growth, first ed. In: *Interdisciplinary Applied Mathematics*, vol. 45, Springer-Verlag, New York, <http://dx.doi.org/10.1007/978-0-387-87710-5>, URL: <https://link.springer.com/book/10.1007/978-0-387-87710-5>.
- Goriely, A., Budday, S., Kuhl, E., 2015. Neuromechanics: From neurons to brain. In: *Advances in Applied Mechanics*, vol. 48, Academic Press Inc., pp. 79–139. <http://dx.doi.org/10.1016/bs.aams.2015.10.002>.
- Goriely, A., Moulton, D.E., Mihai, L.A., 2023. A rod theory for liquid crystalline elastomers. *J. Elasticity* 153, 509–532. <http://dx.doi.org/10.1007/s10659-021-09875>, URL: <https://link.springer.com/article/10.1007/s10659-021-09875-z>.
- Hentschel, H.G., Van Ooyen, A., 1999. Models of axon guidance and bundling during development. *Proc. R. Soc. B: Biol. Sci.* 266, 2231–2238. <http://dx.doi.org/10.1098/rspb.1999.0913>.
- Holland, M.A., Miller, K.E., Kuhl, E., 2015. Emerging brain morphologies from axonal elongation. *Ann. Biomed. Eng.* 43, 1640–1653. <http://dx.doi.org/10.1007/s10439-015-1312-9>.
- Hwu, C., 2010. Infinite Space, Half-Space, and Bimaterials. Springer US, Boston, MA, pp. 87–113. http://dx.doi.org/10.1007/978-1-4419-5915-7_4, (Chapter 4).
- Isomursu, A., Park, K.Y., Hou, J., Cheng, B., Mathieu, M., Shamsan, G.A., Fuller, B., Kasim, J., Mahmoodi, M.M., Lu, T.J., Genin, G.M., Xu, F., Lin, M., Distefano, M.D., Ivaska, J., Odde, D.J., 2022. Directed cell migration towards softer environments. *Nat. Mater.* 21, 1081–1090. <http://dx.doi.org/10.1038/s41563-022-01294-2>, URL: <https://www.nature.com/articles/s41563-022-01294-2>.
- Koch, D., Rosoff, W.J., Jiang, J., Geller, H.M., Urbach, J.S., 2012. Strength in the periphery: growth cone biomechanics and substrate rigidity response in peripheral and central nervous system neurons. *Biophys. J.* 102, 452–460. <http://dx.doi.org/10.1016/j.bpj.2011.12.025>.
- Koser, D.E., Thompson, A.J., Foster, S.K., Dwivedy, A., Pillai, E.K., Sheridan, G.K., Svoboda, H., Viana, M., Costa, L.da.Fountoura, Guck, J., Holt, C.E., Franze, K., 2016. Mechanosensing is critical for axon growth in the developing brain. *Nature Neurosci.* 19 (1592), <http://dx.doi.org/10.1038/nn.4394>.
- Kovács, M., Tóth, J., Hetényi, C., Málnási-Csizmadia, A., Sellers, J.R., 2004. Mechanism of blebbistatin inhibition of myosin II. *J. Biol. Chem.* 279, 35557–35563. <http://dx.doi.org/10.1074/jbc.M405319200>, URL: <https://www.sciencedirect.com/science/article/pii/S0021925820731376>.
- Lamoureux, P., Buxbaum, R.E., Heidemann, S.R., 1989. Direct evidence that growth cones pull. *Nature* 340, 159–162. <http://dx.doi.org/10.1038/340159a0>, URL: <https://www.nature.com/articles/340159a0>.
- Lang, G.E., Waters, S.L., Vella, D., Goriely, A., 2017. Axonal buckling following stretch injury. *J. Elasticity* 129, 239–256. <http://dx.doi.org/10.1007/s10659-016-9604-3>.
- Lin, C.H., Espreafico, E.M., Mooseker, M.S., Forscher, P., 1996. Myosin drives retrograde f-actin flow in neuronal growth cones. *Neuron* 16, 769–782. [http://dx.doi.org/10.1016/S0896-6273\(00\)80097-5](http://dx.doi.org/10.1016/S0896-6273(00)80097-5).
- Maskery, S., Shinbrot, T., 2005. Deterministic and stochastic elements of axonal guidance. *Annu. Rev. Biomed. Eng.* 7, 187–221. <http://dx.doi.org/10.1146/annurev.bioeng.7.060804.100446>, URL: <https://www.annualreviews.org/content/journals/10.1146/annurev.bioeng.7.060804.100446>.
- McCormick, L.E., Gupton, S.L., 2020. Mechanistic advances in axon pathfinding. *Curr. Opin. Cell Biol.* 63, 11–19. <http://dx.doi.org/10.1016/j.ceb.2019.12.003>, URL: <https://www.sciencedirect.com/science/article/pii/S0955067419301139>.
- Miller, K.E., Suter, D.M., 2018. An integrated cytoskeletal model of neurite outgrowth. *Front. Cell. Neurosci.* 12 (447), <http://dx.doi.org/10.3389/fncel.2018.00447>.
- Mortimer, D., Fothergill, T., Pujic, Z., Richards, L.J., Goodhill, G.J., 2008. Growth cone chemotaxis. *Trends Neurosci.* 31, 90–98. <http://dx.doi.org/10.1016/j.tins.2007.11.008>.
- Moulton, D.E., Oliveri, H., Goriely, A., 2020. Multiscale integration of environmental stimuli in plant tropism produces complex behaviors. *Proc. Natl. Acad. Sci. USA* 117, 32226–32237. <http://dx.doi.org/10.1073/pnas.2016025117>.
- Nguyen, T.D., Hogue, I.B., Cung, K., Purohit, P.K., McAlpine, M.C., 2013. Tension-induced neurite growth in microfluidic channels. *Lab A Chip* 13, 3735–3740. <http://dx.doi.org/10.1039/C3LC50681A>, URL: <https://pubs.rsc.org/en/content/articlelanding/2013/lc/c3lc50681a>.
- Nicolas, A., Besser, A., Safran, S.A., 2008. Dynamics of cellular focal adhesions on deformable substrates: consequences for cell force microscopy. *Biophys. J.* 95, 527–539. <http://dx.doi.org/10.1529/biophysj.107.127399>.
- Oliveri, H., De Rooij, R., Kuhl, E., Goriely, A., 2022. Rheology of growing axons. *Phys. Rev. Res.* 4, 033125. <http://dx.doi.org/10.1103/PhysRevResearch.4.033125>, URL: <https://link.aps.org/doi/10.1103/PhysRevResearch.4.033125>.
- Oliveri, H., Franze, K., Goriely, A., 2021. Theory for durotactic axon guidance. *Phys. Rev. Lett.* 126, 118101. <http://dx.doi.org/10.1103/PhysRevLett.126.118101>.
- Oliveri, H., Goriely, A., 2022. Mathematical models of neuronal growth. *Biomech. Model. Mechanobiol.* 21, 89–118. <http://dx.doi.org/10.1007/S10237-021-01539-0>, URL: <https://link.springer.com/article/10.1007/s10237-021-01539-0>.
- O'Toole, M., Lamoureux, P., Miller, K.E., 2008. A physical model of axonal elongation: Force, viscosity, and adhesions govern the mode of outgrowth. *Biophys. J.* 94, 2610–2620. <http://dx.doi.org/10.1529/biophysj.107.117424>, URL: [https://www.cell.com/biophysj/fulltext/S0006-3495\(08\)70514-9](https://www.cell.com/biophysj/fulltext/S0006-3495(08)70514-9).

- O'Toole, M., Miller, K.E., 2011. The role of stretching in slow axonal transport. *Biophys. J.* 100, 351–360. <http://dx.doi.org/10.1016/j.bpj.2010.12.3695>, URL: [https://www.cell.com/biophysj/fulltext/S0006-3495\(10\)05210-0](https://www.cell.com/biophysj/fulltext/S0006-3495(10)05210-0).
- Press, W.H., Teukolsky, S.A., Vetterling, W.T., Flannery, B.P., 2007. *Numerical Recipes: The Art of Scientific Computing*, third ed. Cambridge University Press, New York, URL: <https://www.cambridge.org/de/universitypress/subjects/mathematics/numerical-recipes/numerical-recipes-art-scientific-computing-3rd-edition>.
- Purohit, P.K., Smith, D.H., 2016. A model for stretch growth of neurons. *J. Biomech.* 49, 3934–3942. <http://dx.doi.org/10.1016/j.jbiomech.2016.11.045>, URL: <https://www.sciencedirect.com/science/article/pii/S0021929016312246>.
- Raffa, V., 2023. Force: A messenger of axon outgrowth. *Semin. Cell & Dev. Biology* 140, 3–12. <http://dx.doi.org/10.1016/j.semcdb.2022.07.004>, URL: <https://www.sciencedirect.com/science/article/pii/S1084952122002336>.
- Recho, P., Jérusalem, A., Goriely, A., 2016. Growth, collapse, and stalling in a mechanical model for neurite motility. *Phys. Rev. E* 93, <http://dx.doi.org/10.1103/PhysRevE.93.032410>, URL: <https://journals.aps.org/pre/abstract/10.1103/PhysRevE.93.032410>.
- Sabass, B., Schwarz, U.S., 2010. Modeling cytoskeletal flow over adhesion sites: competition between stochastic bond dynamics and intracellular relaxation. *J. Phys.: Condens. Matter* 22, 194112. <http://dx.doi.org/10.1088/0953-8984/22/19/194112>.
- Sáez, P., Venturini, C., 2023. Positive, negative and controlled durotaxis. *Soft Matter* 19, 2993–3001. <http://dx.doi.org/10.1039/D2SM01326F>, URL: <https://pubs.rsc.org/en/content/articlelanding/2023/sm/d2sm01326f>.
- Santos, T.E., Schaffran, B., Broguière, N., Meyn, L., Zenobi-Wong, M., Bradke, F., 2020. Axon growth of CNS neurons in three dimensions is amoeboid and independent of adhesions. *Cell Rep.* 32, 107907. <http://dx.doi.org/10.1016/j.celrep.2020.107907>, URL: <https://www.sciencedirect.com/science/article/pii/S2211124720308883>.
- Schaeffer, J., Weber, I.P., Thompson, A.J., Keynes, R.J., Franze, K., 2022. Axons in the chick embryo follow soft pathways through developing somite segments. *Front. Cell Dev. Biol.* 10, <http://dx.doi.org/10.3389/fcell.2022.917589>, URL: <https://www.frontiersin.org/articles/10.3389/fcell.2022.917589>.
- Sens, P., 2013. Rigidity sensing by stochastic sliding friction. *Europhys. Lett.* 104, 38003. <http://dx.doi.org/10.1209/0295-5075/104/38003>, URL: <https://iopscience.iop.org/article/10.1209/0295-5075/104/38003>.
- Shellard, A., Mayor, R., 2021. Durotaxis: The hard path from in vitro to in vivo. *Dev. Cell* 56, 227–239. <http://dx.doi.org/10.1016/j.devcel.2020.11.019>, URL: <https://www.sciencedirect.com/science/article/pii/S153458072030928X>.
- Silk, W.K., Erickson, R.O., 1979. Kinematics of plant growth. *J. Theoret. Biol.* 76, 481–501. [http://dx.doi.org/10.1016/0022-5193\(79\)90014-6](http://dx.doi.org/10.1016/0022-5193(79)90014-6), URL: <https://www.sciencedirect.com/science/article/pii/0022519379900146>.
- Smeal, R.M., Rabbitt, R., Biran, R., Tresco, P.A., 2005. Substrate curvature influences the direction of nerve outgrowth. *Ann. Biomed. Eng.* 33, 376–382. <http://dx.doi.org/10.1007/s10439-005-1740-z>, URL: <https://link.springer.com/article/10.1007/s10439-005-1740-z>.
- Šmít, D., Fouquet, C., Pincet, F., Zapotocky, M., Trembleau, A., 2017. Axon tension regulates fasciculation/defasciculation through the control of axon shaft zippering. *eLife* 6, <http://dx.doi.org/10.7554/eLife.19907>, URL: <https://elifesciences.org/articles/19907>.
- Srinivasan, M., Walcott, S., 2009. Binding site models of friction due to the formation and rupture of bonds: state-function formalism, force-velocity relations, response to slip velocity transients, and slip stability. *Phys. Rev. E* 80, 046124. <http://dx.doi.org/10.1103/PhysRevE.80.046124>, URL: <https://journals.aps.org/pre/abstract/10.1103/PhysRevE.80.046124>.
- Suter, D.M., Miller, K.E., 2011. The emerging role of forces in axonal elongation. *Prog. Neurobiol.* 94, 91–101. <http://dx.doi.org/10.1016/j.pneurobio.2011.04.002>, URL: <https://www.sciencedirect.com/science/article/pii/S0301008211000530>.
- Thompson, A.J., Pillai, E.K., Dimov, I.B., Foster, S.K., Holt, C.E., Franze, K., 2019. Rapid changes in tissue mechanics regulate cell behaviour in the developing embryonic brain. *eLife* 8, e39356. <http://dx.doi.org/10.7554/eLife.39356>, URL: <https://elifesciences.org/articles/39356>.
- Trefethen, L.N., 2000. *Spectral Methods in MATLAB*. SIAM, <http://dx.doi.org/10.1137/1.9780898719598>, URL: <https://epubs.siam.org/doi/book/10.1137/1.9780898719598>.
- Turney, S.G., Bridgman, P.C., 2005. Laminin stimulates and guides axonal outgrowth via growth cone myosin II activity. *Nature Neurosci.* 8, 717–719. <http://dx.doi.org/10.1038/nn1466>, URL: <https://www.nature.com/articles/nn1466>.
- Wolpert, L., 2008. The french flag problems a contribution to the discussion on pattern development and regulation. In: Waddington, C.H. (Ed.), *The Origin of Life*. vol. 1, Routledge, pp. 125–133. <http://dx.doi.org/10.4324/9781315133638-12>, URL: <https://www.taylorfrancis.com/chapters/edit/10.4324/9781315133638-12/>.